Title
Consequences of a solid inner core on Mercury's spin configuration

Authors
Peale, Stanton J
Margot, Jean-Luc
Hauck, Steven A
et al.

Publication Date
2016

DOI
10.1016/j.icarus.2015.09.024

Peer reviewed

Consequences of a solid inner core on Mercury's spin configuration

Stanton J. Peale[a,1], Jean-Luc Margot[b,c], Steven A. Hauck, II[d], Sean C. Solomon[e,f]

[a]Department of Physics, University of California, Santa Barbara, CA 93106.
[b]Department of Earth, Planetary, and Space Sciences, University of California, Los Angeles CA 90095.
[c]Department of Physics and Astronomy, University of California, Los Angeles, CA 90095.
[d]Department of Earth, Environmental, and Planetary Sciences, Case Western Reserve University, Cleveland, OH 44106.
[e]Department of Terrestrial Magnetism, Carnegie Institution of Washington, Washington, DC 20015.
[f]Lamont-Doherty Earth Observatory, Columbia University, Palisades, NY 10964.

Abstract

The pressure torque by a liquid core that drove Mercury to the nominal Cassini state of rotation is dominated by the torque from the solid inner core. The gravitational torque exerted on Mercury's mantle from an asymmetric solid inner core increases the equilibrium obliquity of the mantle spin axis. Since the observed obliquity of the mantle must be compatible with a solid inner core of any size, the moment of inertia inferred from the occupancy of the Cassini state must be reduced to compensate the torque from the inner core and bring Mercury's spin axis to the observed position. The unknown size and shape of the inner core means that the moment of inertia is more uncertain than previously inferred.

[1]Deceased 14 May 2015

1. Introduction

Mercury is in a stable spin–orbit resonance in which the rotational angular velocity is precisely 1.5 times the mean orbital motion (Pettengill and Dyce 1965; Colombo and Shapiro 1966). This rotation state is a natural outcome of tidal evolution (Goldreich and Peale 1966) or other dissipative effects, although the details of the resonance capture mechanism are still debated (Correia and Laskar 2004, 2009; Wieczorek et al. 2012; Correia and Laskar 2012; Noyelles et al. 2014). In addition, the same dissipation brings Mercury to Cassini state 1, wherein Mercury's spin axis remains coplanar with the orbit normal and Laplace plane normal as the spin vector and orbit normal precess around the latter with a $\sim 300,000$ yr period (Colombo 1966; Peale 1969, 1974). Because the Laplace plane is itself variable on long time scales, one can invoke an instantaneous Laplace plane that is valid at the present epoch (Yseboodt and Margot 2006). On the basis of theoretical calculations, Mercury is expected to remain close to the Cassini state (Peale 2006). That Mercury is very close to this state has been verified with radar observations, which give an obliquity of 2.04 ± 0.08 arcmin (Margot et al. 2007, 2012), consistent with analysis of MESSENGER spacecraft gravity data, laser altimetry, and stereo digital terrain models (Mazarico et al. 2014; Stark et al. 2015). The most recent observations show that the best-fit solutions are offset from the Cassini state by a few arcseconds, but the uncertainty at one standard deviation includes the Cassini state.

Pressure torque between Mercury's fluid core and its mantle drive Mercury's spin axis to the Cassini state (Peale et al. 2014) (hereinafter Paper 1). It thereby dominates dissipative viscous, topographic, and magnetic effects that would otherwise result in significant displacement of the observable spin axis from the Cassini state position. This result is reassuring as Mercury's spin is observed to occupy the Cassini state (Margot et al. 2007, 2012; Mazarico et al. 2014; Stark et al. 2015), but at the same time it frustrates the establishment of any constraints on Mercury's interior that could result from a measurable displacement. We show here that the increase in the obliquity from torques exerted by an asymmetric solid inner core can be reversed by the reduction of Mercury's polar moment of inertia from the value inferred if there is no inner core. For a small inner core, the current best estimate of the moment of inertia would be unchanged, but for a large inner core, the revised estimate would be smaller than the current estimate.

The assumed model of the planet consists of four homogeneous layers: crust, mantle, fluid outer core, and solid inner core (Fig. 1). R_i and ρ_i designate the radii and densities of the various layers, with subscript c for crust, m for mantle, f for fluid outer core, and s for solid inner core. $R_c = 2440$ km is the measured planetary radius, and the selected value

of ρ_c is described below. The crustal thickness is specified by the choice of R_m. The inner core ρ_s and R_s are also specified. We will evolve the spin configuration for three values of ρ_s (8.0, 9.3, and 10.0 g/cm^3) to span the uncertainty in this value. Five inner core radii will be assumed (0.0 or no inner core, 0.3, 0.4, 0.5, and 0.6 R_c, where R_c should not be confused with R_f). The densities ρ_f, ρ_m along with the radius R_f of the core–mantle boundary (CMB) will be solved to produce the known values of the total planetary mass m, the total moment of inertia C/mR_c^2, and the moment of inertia of the mantle–crust alone $(C_m + C_c)/C$.

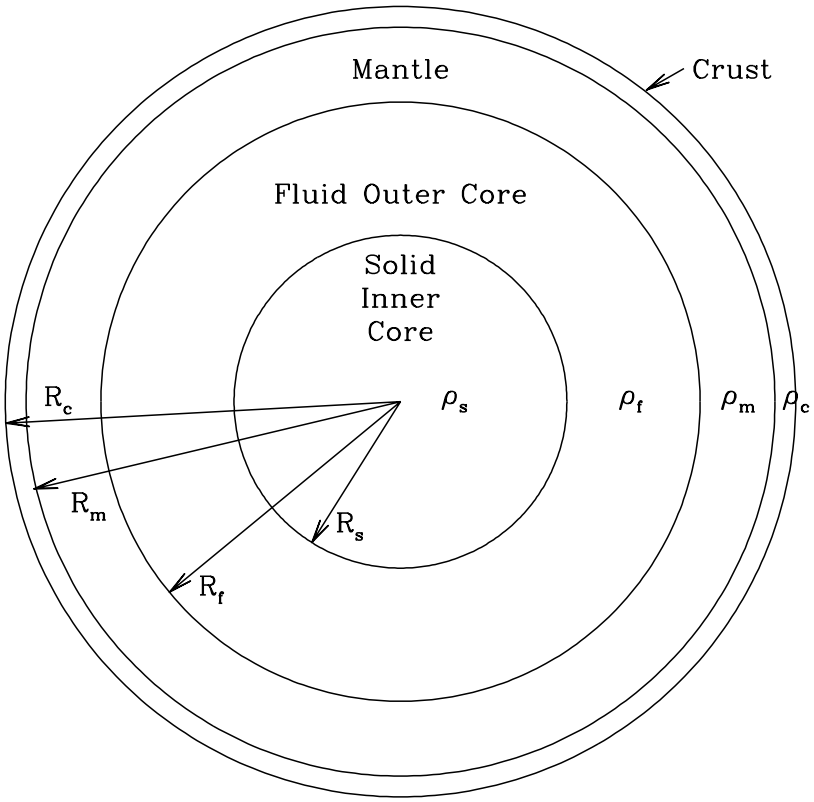

Fig. 1.— Model of Mercury's interior as four concentric and homogeneous layers. Note that in our notation R_c is the radius of the crust, which is that of the planet. This symbol is often used in other publications to indicate the radius of the fluid core, which in our notation is R_f. We assume $R_c = 2440\,\mathrm{km}$ and $\rho_c = 2.8\,\mathrm{g/cm^3}$ in all our calculations.

The second-degree zonal and tesseral spherical harmonic gravitational coefficients J_2 and C_{22} can be expressed in terms of the densities and radii of the layers and their ellipticities. The ellipticities of the top of the crust have been measured; the mean polar ellipticity

$\epsilon_c = 5.534 \times 10^{-4}$ and the equatorial ellipticity $\xi_c = 4.919 \times 10^{-4}$ (Perry et al. 2015). Expressions for J_2 and C_{22} along with relations for the assumed equipotential surfaces at the CMB and inner core boundary (ICB) provide a sufficient number of equations to solve for all the remaining ellipticities, which change with a change in the assumed inner core radius. The ellipticities are required to calculate the torques. We will neglect the $\sim 15^\circ$ misalignment of the equatorial long axis and the $\sim 6^\circ$ misalignment of the short axis of the crust with those of the geoid as determined by MESSENGER laser altimetry and radio occultations (Perry et al. 2015).

In Section 2 we write the general dynamical equations that are derived in Paper 1. Although written for the mantle–crust combination, they apply to the other two layers representing the fluid core and the solid inner core with a change in the subscripts of the parameters. There are three sets of equations that must be solved simultaneously to map the evolution of the system equations for the combined crust and mantle and the outer and inner core to the equilibrium configuration. The various torques to be used in the equations are developed in several subsections. The ICB will be at least gravitationally distorted by the non-radial internal field of the mantle–crust and fluid outer core and less so by the solar and rotational fields (Paper 1). We include the mutual gravitational torques that result from any misalignment of the ellipsoidal shape of the inner core with that of the mantle. This torque is sustained since the inner core obliquity remains larger than the mantle obliquity in equilibrium. We consider this mutual torque along with the direct solar gravitational torques acting on each of the three layers, the mantle–crust, the fluid outer core, and the solid inner core. The first is considered a single layer for the dynamical equations, since mantle and crust move together. Pressure torques acting at the CMB and at the ICB include those induced by gravity and by the fluid velocity at the ICB and CMB. A viscous interaction provides a dissipative evolution to an equilibrium configuration whereby the spin axes of the respective layers remain fixed in a frame precessing with the orbit. The torques from tides, magnetic coupling, and topographic coupling treated in Paper 1 are small and do not affect the evolution to the equilibrium state. These latter torques are therefore not included here.

We chose a crustal density $\rho_c = 2.8\,\mathrm{g/cm^3}$, which we maintain for all of the calculations. This choice is based on results from the Moon, where the mean crustal density is 2.6 $\mathrm{g/cm^3}$, which implies considerable porosity (12%) (Wieczorek et al. 2013). The lunar crustal density approaches 2.4 $\mathrm{g/cm^3}$ at the shallowest depths. The $2.8\,\mathrm{g/cm^3}$ chosen for Mercury's crust can then account for Mercury's higher surface gravitational acceleration and perhaps a lower porosity. The inner core density is arbitrary except that $\rho_s = 8$ $\mathrm{g/cm^3}$ is taken as a lower limit to possible values. That the mantle–crust obliquity decreases with C/mR_c^2 suggests that by reducing C/mR_c^2 we can compensate for the increased obliquity caused by the interaction

between the mantle–crust and the inner core. When the moment of inertia is that which is appropriate for no inner core, the mantle obliquity is displaced to larger and larger obliquities as the inner core size increases. The mantle obliquity is matched to within the observational uncertainty by appropriate reductions in C/mR_c^2 for each core size. These reductions increase as the inner core size increases. Some of the models obtained for the range of inner core densities are unlikely.

The results are detailed in Section 3 for the ranges of inner core sizes and densities considered. We show that for an ICB and a CMB that are equipotential surfaces, the equilibrium position of the mantle spin is displaced toward obliquities higher than that of the Cassini state appropriate to Mercury with no solid inner core and therefore higher than the observed obliquity. We demonstrate below that the required reductions in C/mR_c^2 are significant for $R_s > 0.3R_c$. The displacement of the evolved mantle spins from the Cassini state for the unaltered $C/mR_c^2 = 0.346$ determined from the observed obliquity and deduced for Mercury with a fluid core but no solid inner core is shown for $\rho_s = 8.0\,\mathrm{g/cm^3}$ only. The restoration of the evolved mantle-crust spin to the observed position for all three inner core densities is shown with appropriate reductions in C/mR_c^2.

The mantle–crust obliquity increases with the inner core size. The displacement vanishes if the direct gravitational torque between the mantle and inner core is set to zero. The obliquity is used to determine the moment of inertia of Mercury (e.g., Peale et al. 2014). The increase in the obliquity of the mantle from gravitational torques due to the inner core means that C/mR_c^2 must be reduced by an amount that increases with inner core radius to bring the mantle spin back to the observed position. We discuss the implications in Section 4 where the values of C/mR_c^2 versus R_s, the radius of the solid inner core, are given. This exercise is repeated for inner core densities of 9.3 g/cm^3 and 10.0 g/cm^3.

2. Equations of variation

The coordinate systems and angles for the equations that govern the rotational motion of Mercury are shown in Fig. 2, where X', Y', Z' are quasi-inertial axes with the $X'Y'$ plane being the Laplace plane on which Mercury's orbit precesses at nearly a constant inclination I and nearly constant angular velocity $\boldsymbol{\mu} = -\mu \mathbf{k}_L$ ($\mathbf{k}_L$=normal to Laplace plane). The XYZ orbit system has the X axis along the ascending node of the orbit plane on the Laplace plane, and the XY plane is the orbit plane. The xyz system is fixed in the body, with z along the spin axis and x along the axis of minimum moment of inertia in the equator plane. The Euler angles orienting the xyz system relative to the XYZ system are Ω, i, ψ, where Ω

is the longitude of the ascending node of the equator plane on the XY orbit plane measured from the X axis, i is the inclination of the equator plane to the orbit plane, and ψ is the angle from the ascending node of the equator on the orbit plane to the x axis of minimum moment of inertia. The three Euler angles and the body coordinates will have subscripts m, f, or s to designate mantle–crust, fluid core, or solid inner core, respectively, as in Paper 1. We use subscript c when we refer to the crust alone. Angle I is the inclination of the orbit plane to the Laplace plane, Ω_o is the longitude of the ascending node of the orbit plane on the Laplace plane, ω is the argument of perihelion, f is the true anomaly of the Sun, and r is the distance from Mercury to the Sun.

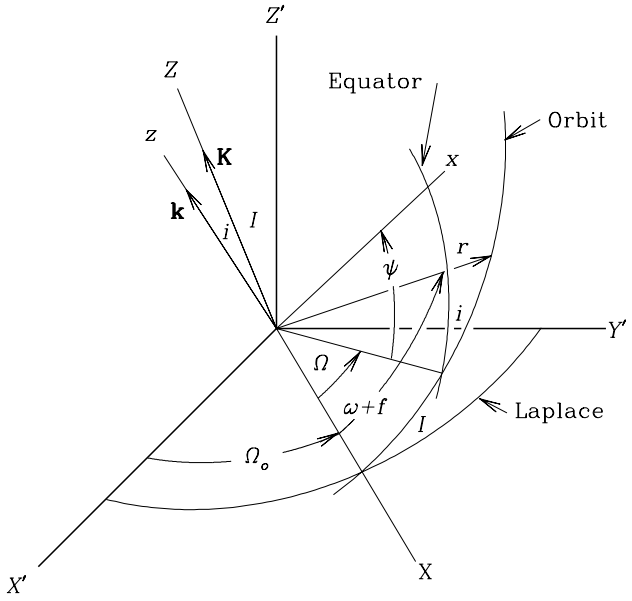

Fig. 2.— Coordinate systems and relevant angles. The Euler angles orienting the body-fixed xyz system relative to the orbit XYZ system are Ω, i, and ψ. These angles as well as the xyz coordinates will have subscripts m, f, or s for mantle–crust, fluid core, and solid inner core, respectively.

We assume principal axis rotation for all three layers throughout, in part because free

rotational modes of the mantle and crust are expected to damp on relatively short ($\sim 10^5$ y) time scales (Peale 2005). Following Paper 1, we arrive at the following for the variation of the Euler angles orienting the mantle frame relative to the orbit frame of reference:

$$\begin{aligned}
\frac{d\dot{\psi}_m}{dt} &= p_m N_{mX} - q_m N_{mY} + \sqrt{1-p_m^2-q_m^2}\,N_{mZ} \\
\frac{dp_m}{dt} &= \frac{1}{\dot{\psi}_m}\left[(1-p_m^2)N_{mX} + p_m q_m N_{mY} - p_m\sqrt{1-p_m^2-q_m^2}\,N_{mZ}\right] \\
\frac{dq_m}{dt} &= -\frac{1}{\dot{\psi}_m}\left[p_m q_m N_{mX} + (1-q_m^2)N_{mY} + q_m\sqrt{1-p_m^2-q_m^2}\,N_{mZ}\right], \qquad (1)
\end{aligned}$$

where N_{mi} are the components of $\mathbf{N}_m$ in the XYZ orbit frame of reference with

$$\begin{aligned}
\mathbf{N}_m &= \frac{\langle \mathbf{T}_m \rangle}{C_m + C_c} - \boldsymbol{\mu} \times \dot{\boldsymbol{\psi}}_{\boldsymbol{m}}, \\
p_m &= \sin i_m \sin \Omega_m, \\
q_m &= \sin i_m \cos \Omega_m, \qquad (2)
\end{aligned}$$

where $\mathbf{T_m}$ is the total torque on the mantle–crust and the angled brackets indicate an average over the orbit. In Eq. (2), $\boldsymbol{\mu}$ is the orbit precession angular velocity. The equations for the fluid and solid core motions are identical to Eqs. (1) and (2) with subscripts changed to f and s, respectively. The evolution of the spin state is governed by the solution of the set of nine equations under the action of appropriate torques the forms of which we now determine.

2.1. Solar gravitational torque

The averaged solar torque on the mantle was developed in Paper 1 with the result

$$\begin{aligned}
\frac{\langle \mathbf{T}^m_{solar} \rangle_X}{C_m + C_c} &= -\frac{n^2}{\alpha_m}\left[\frac{3}{2} J_2 \sin i_m \cos i_m \cos \Omega_m g_1(e)\right. \\
&\quad + \frac{3}{2} C_{22} \sin i_m (1 + \cos i_m) \cos(\Omega_m - 2\gamma) g_2(e) \\
&\quad \left. + \frac{3}{2} C_{22} \sin i_m (1 + \cos i_m) \cos(2\omega - \Omega_m + 2\gamma) g_3(e)\right], \\
\frac{\langle \mathbf{T}^m_{solar} \rangle_Y}{C_m + C_c} &= -\frac{n^2}{\alpha_m}\left[\frac{3}{2} J_2 \sin i_m \cos i_m \sin \Omega_m g_1(e)\right. \\
&\quad + \frac{3}{2} C_{22} \sin i_m (1 + \cos i_m) \sin(\Omega_m - 2\gamma) g_2(e) \\
&\quad \left. - \frac{3}{2} C_{22} \sin i_m (1 + \cos i_m) \sin(2\omega - \Omega_m + 2\gamma) g_3(e)\right], \\
\frac{\langle \mathbf{T}^m_{solar} \rangle_Z}{C_m + C_c} &= -\frac{n^2}{\alpha_m}\left\{\frac{3}{2} C_{22} (1 + \cos i_m)^2 \left[g_2(e) \sin 2\gamma + g_4(e) \sin(4\omega - 4\Omega_m + 2\gamma)\right]\right\}, \quad (3)
\end{aligned}$$

where the moment of inertia of the mantle–crust $C_m + C_c = \alpha_m m R_c^2$ defines α_m and $n^2 = Gm_\odot/a^3$ has been used with n = orbital mean motion, G = gravitational constant, $m_\odot$ = solar mass, and a = orbital semimajor axis. The choice of $C_m + C_c$ in Eqs. (3) means they apply to the mantle–crust alone, and the second-degree gravitational harmonic coefficients J_2 and C_{22} correspond only to this part of Mercury. The averaged solar gravitational torque on the solid inner core $\langle \mathbf{T}^s_{solar} \rangle / C_s$ is the same as Eqs. (3) with subscripts m replaced by s. In Paper 1 it was shown that the gravitationally induced pressure torque on the CMB adds to the direct gravitational torque as if the thin ellipsoidal shell of core fluid that protrudes into the mantle is added to the mantle. The contributions of the fluid core are therefore included in the values of J_2 and C_{22} in Eq. (3). We show in Appendix A that the pressure torque on the inner core due to the gravity field opposes the direct gravitational torque such that the effective torque is the same as the direct gravity on a body with the shape of the inner core, but with a density $\rho_s - \rho_f$, where ρ_s, ρ_f are the densities of the inner core and fluid core, respectively.

In Eqs. (3)

$$\begin{aligned} g_1(e) &= (1-e^2)^{-3/2} \\ g_2(e) &= \frac{7e}{2} - \frac{123e^3}{16} + \frac{489e^5}{128} + ... \\ g_3(e) &= \frac{53e^3}{16} + \frac{393e^5}{256} + ... \\ g_4(e) &= \frac{85e^5}{2560} + ..., \end{aligned} \tag{4}$$

where e is the orbital eccentricity. There are additional terms in the X and Y components of $\mathbf{T}^m_{solar}$ to order e^5 with factors $\sin i_m(1-\cos i_m)$. Since Mercury's obliquity is about 2 arcmin (Margot et al. 2007, 2012) and since we always start the integrations close to the final state, these factors coupled with lowest-order factors of e^3 or e^5 make these terms negligibly small compared with the terms that are retained. With fluid core and inner core parameters, Eqs. (3) apply to the fluid and inner core as well, but we show below that pressure forces between fluid core and mantle and separately the inner core effectively cancel the gravitational torque on the fluid outer core.

2.2. Gravitational torque on the inner core from the mantle

If $a > b > c$ are the three semiaxes, an ellipsoidal surface is represented by $x^2/a^2+y^2/b^2+z^2/c^2 = 1$ or $x^2 + y^2/(1-\xi)^2 + z^2/(1-\epsilon_a)^2 = a^2$, where $\epsilon_a = (a-c)/a$ and $\xi = (a-b)/a$. If we write (x, y, z) in terms of spherical polar coordinates (radius r, colatitude θ, longitude ϕ),

$$\frac{r}{a} = 1 - \left(\frac{\epsilon_a}{3} + \frac{\xi}{3}\right) - \left(\frac{2\epsilon_a}{3} - \frac{\xi}{3}\right) P_{20}(\cos\theta) + \frac{\xi}{6} P_{22}(\cos\theta)\cos 2\phi, \tag{5}$$

to first order in ϵ_a and ξ where P_{20} and P_{22} are Legendre functions. The coefficient of P_{20} can be written $(-2/3)(\epsilon_a/2+\epsilon_b/2) = (-2/3)\epsilon$, where $\epsilon_b = (b-c)/a$ and ϵ is thereby a mean polar ellipticity. Then

$$\frac{r}{a} = 1 - \left(\frac{\epsilon}{3} + \frac{\xi}{2}\right) - \frac{2}{3}\epsilon P_{20}(\cos\theta) + \frac{\xi}{6} P_{22}(\cos\theta)\cos 2\phi, \tag{6}$$

where the ellipsoidal surface is characterized by the ellipticities ϵ and ξ. As noted above, we model Mercury as four homogeneous layers with densities ρ_c, ρ_m, ρ_f, and ρ_s for the crust, mantle, fluid outer core, and solid inner core, respectively. The surface of each layer is distinguished by placing the same subscripts on the two ellipticities. The crust and mantle

are rigidly attached and move together, but the mutual torques are calculated separately for the crust and mantle.

We shall first assume an inner core density of 8 g/cm^3 or slightly above and several values for the inner core radius. With these assumptions, the three quantities ρ_m, ρ_f, and R_f, the radius of the fluid core (CMB), can be determined to be consistent with measured values of C/mR_c^2, $(C_m + C_c)/C$, and total mass m, where $C_m + C_c$ is the polar moment of inertia of the mantle–crust. The observed values of the second degree gravitational coefficients, J_2 and C_{22}, can be expressed as a sum of contributions from the ellipsoidal shapes of the surfaces of each layer (*e.g.,* Paper 1). Equipotential surfaces at the CMB and the ICB give additional relations among the ellipticities. The known parameters are $J_2 = 5.03 \times 10^{-5}$, $C_{22} = 0.809 \times 10^{-5}$, $C/mR_c^2 = 0.346$, $(C_m + C_c)/C = 0.431$, and $m = 3.301 \times 10^{26}$g, where C/mR_c^2 and $(C_m+C_c)/C$ are the values derived assuming that there is no solid inner core. (We show below that C/mR_c^2 must be reduced and $(C_m + C_c)/C$ increased when there is an elliptical solid inner core.) The values of J_2, C_{22}, and m come from Smith et al. (2012) and Mazarico et al. (2014), and C/mR_c^2 and $(C_m + C_c)/C$ from Margot et al. (2012). In summary there are 16 unknowns (4ϵs, 4ξs, 4ρs, and 4Rs) and 10 equations (C/mR^2, $(C_m + C_c)/C$, m, R_c, J_2, C_{22}, two equipotential surface conditions at the CMB, and two at the ICB). Our specification of $R_m = 2390$ km yields a crustal thickness of 50 km. Padovan et al. (2015) found a crustal thickness near 35 km, although 50 km is within their uncertainty at one standard deviation. There was a negligible change in the evolution if 35 km was used instead of 50 km. With the four specified values of the parameters, ρ_s, R_s, ρ_c, and R_m and the measured values $\epsilon_c = 5.534 \times 10^{-4}$ and $\xi_c = 4.919 \times 10^{-4}$ (Perry et al. 2015) the number of unknowns is reduced to 10. The procedure for solution was carried out in Appendix A of Paper 1 for a three-layer model. One only need add terms to Eqs. (41) in that paper to accommodate the crust, and the set is solvable for R_f, ρ_f, ρ_m as before to yield the observables. The ellipticities follow as in Paper 1, except now there are additional ellipticities at the crust–mantle boundary.

The major contrast from the $\rho_s = 8.0$ g/cm^3 case for $\rho_s = 9.3$ and 10.0 g/cm^3 is a much larger difference between the density of the inner core and that of the fluid outer core, which may be more likely given the change in phase at the ICB and the probable light elements (e.g., S, Si) in the fluid core (Hauck II et al. 2013). The details of these models, e.g., densities and CMB radii, are displayed in Table 1. The final obliquities of each part of Mercury are also included. The inner core obliquity is separated from the mantle–crust obliquity more than the equilibrium fluid core obliquity for all sets of parameters. The precession causes the difference in obliquities to be maintained in equilibrium, leading to a maintained torque between the mantle–crust and the inner core. The fluid outer core obliquity usually falls

between that of the mantle–crust and that of the inner core, but not always. The inner core density was chosen to be 8.05 g/cm^3 instead of 8.0 g/cm^3 on the fifth line of the first part of Table 1 to force the fluid core density to be less than that of the inner core. A model with $\rho_f > \rho_s$ seems immediately rejectable.

If we multiply Eq. (6) by a, subtract the constant term on the right-hand side from both sides, and replace a by the mean radius, which we call R_m, R_f, and R_s for the three surfaces, an expression for the deviation of the radius of the surface from a sphere Δr results. We can then determine the non-radial potential inside and outside the surface mass distribution given by

$$\sigma(\theta,\phi) = -\frac{2}{3}\epsilon R_i \rho P_{20}(\cos\theta) + \frac{\xi}{6} R_i \rho P_{22}(\cos\theta)\cos 2\phi, \tag{7}$$

where the potential interior to the mantle–crust from the surface mass distributions on the inner and outer surfaces of mean radii R_m and R_f is (*e.g.,* Appendix A of Paper 1)

$$\Phi_{int}(r,\theta,\phi) = \frac{8\pi G r^2}{15}[\epsilon_m\rho_m + (\rho_f - \rho_m)\epsilon_f]P_{20}(\cos\theta) - \frac{2\pi G r^2}{15}[\xi_m\rho_m + \xi_f(\rho_f - \rho_m)]P_{22}(\cos\theta)\cos 2\phi. \tag{8}$$

The spherical coordinates are relative to the mantle–crust principal axes, and the inner and outer ellipsoidal surfaces of the mantle are assumed to be aligned. The torque on the inner core from the gravitational field of the mantle for the uniform density layers is given by

$$\mathbf{T}^s_{mantlegrav} = -\iiint_{IC} \mathbf{r} \times (\rho_s - \rho_f)\nabla\Phi_{int} dV, \tag{9}$$

where the fluid core density ρ_f is subtracted because of the pressure force on the inner core surface (demonstrated in Appendix A), and where the integral is over the volume of the inner core. Another way to motivate the density difference at the inner core is to note that the torque must vanish if $\rho_f = \rho_s$. With a homogeneous inner core, the integral can be changed to a surface integral over a surface distribution of mass like Eq. (7) with $(\rho_s - \rho_f)dV \rightarrow (\sigma_s - \sigma_f)dS = (\rho_s - \rho_f)\Delta r_s dS$, since the integral over the interior spherically symmetric distribution of mass vanishes. For each element dS, the integrand of Eq. (9) represents the torque on that element of mass due to the gravitational potential of the mantle. The total torque is the integral over the surface. The asymmetric part of the interior potential due to the mantle can be written $\Phi_{int} = (8\pi G/15)K_a[z_m^2 - (x_m^2 + y_m^2)/2] - (2\pi G/5)K_b(x_m^2 - y_m^2)$ in Cartesian coordinates, where $K_a = \epsilon_m\rho_m + \epsilon_f(\rho_f - \rho_m)$ and $K_b = \xi_m\rho_m + \xi_f(\rho_f - \rho_m)$. With $\mathbf{r}_m = x_m\mathbf{i}_m + y_m\mathbf{j}_m + z_m\mathbf{k}_m$ and $(\mathbf{i}_m, \mathbf{j}_m, \mathbf{k}_m)$ as unit vectors along the principal axes of the mantle, it is easy to obtain

$$\mathbf{r} \times (-\nabla\Phi) = \frac{4\pi}{5} G[-(2K_a - K_b)y_m z_m\,\mathbf{i}_m + (2K_a + K_b)x_m z_m\,\mathbf{j}_m - 2K_b x_m y_m\,\mathbf{k}_m], \tag{10}$$

which yields the components of the torque on the element $(\rho_s - \rho_f)\Delta r_s dS$ along the mantle principal axis directions in terms of the mantle coordinates of the point.

In order to integrate over the surface of the inner core, the mantle coordinates of the point must be expressed in terms of the inner core coordinates. If (ℓ_1, ℓ_2, ℓ_3), (m_1, m_2, m_3), and (n_1, n_2, n_3) comprise the rows of the orthogonal matrix relating the coordinates x_m, y_m, z_m to x_s, y_s, z_s, then $x_m = \ell_1 x_s + \ell_2 y_s + \ell_3 z_s$, $y_m = m_1 x_s + m_2 y_s + m_3 z_s$ and $z_m = n_1 x_s + n_2 y_s + n_3 z_s$. To integrate the torque on the surface mass elements over the spherical surface, we write $x_s = R_s \sin\theta_s \cos\phi_s$, $y_s = R_s \sin\theta_s \sin\phi_s$, $z_s = R_s \cos\theta_s$. Eq. (9) becomes

$$\begin{aligned}
\mathbf{T}^s_{mantlegrav} &= \iint_{ICB} \mathbf{r} \times (-\nabla\Phi)(\sigma_s - \sigma_f) dS \qquad (11)\\
&= \int_0^{\pi}\int_0^{2\pi} \mathbf{r} \times (-\nabla\Phi)(\rho_s - \rho_f)\Big[-\frac{2}{3}\epsilon_s R_s P_{20}(\cos\theta_s)\\
&\quad + \frac{\xi_s}{6} R_s P_{22}(\cos\theta_s)\cos 2\phi_s \Big] R_s^2 \sin\theta_s d\theta_s d\phi_s,
\end{aligned}$$

where Eq.(10) is inserted for $\mathbf{r} \times (-\nabla\Phi)$ with x_m, y_m, z_m expressed in terms of x_s, y_s, z_s through the rotation matrix with components ℓ_i, m_i, n_i. The cross product $r \times (-\nabla\Phi)$ involves products of mantle system coordinates, which become products of inner core coordinates after the transformation. There results

$$\begin{aligned}
\mathbf{T}^s_{mantlegrav} &= -\frac{16}{225} G\pi^2 (\rho_s - \rho_f) R_s^5 \{ (2K_a - K_b)[2\epsilon_s(m_1 n_1 + m_2 n_2 - 2m_3 n_3) + 3\xi_s(m_1 n_1 - m_2 n_2)]\mathbf{i}_m\\
&\quad -(2K_a + K_b)[2\epsilon_s(\ell_1 n_1 + \ell_2 n_2 - 2\ell_3 n_3) + 3\xi_s(\ell_1 n_1 - \ell_2 n_2)]\mathbf{j}_m\\
&\quad +2K_b[2\epsilon_s(\ell_1 m_1 + \ell_2 m_2 - 2\ell_3 m_3) + 3\xi_s(\ell_1 m_1 - \ell_2 m_2)]\mathbf{k}_m\},\\
&= -\frac{16}{75} G\pi^2 (\rho_s - \rho_f) R_s^5 \{ (2K_a - K_b)[-2\epsilon_s m_3 n_3 + \xi_s(m_1 n_1 - m_2 n_2)]\mathbf{i}_m\\
&\quad -(2K_a + K_b)[-2\epsilon_s \ell_3 n_3 + \xi_s(\ell_1 n_1 - \ell_2 n_2)]\mathbf{j}_m\\
&\quad +2K_b[-2\epsilon_s \ell_3 m_3 + \xi_s(\ell_1 m_1 - \ell_2 m_2)]\mathbf{k}_m\}, \qquad (12)
\end{aligned}$$

where the second form follows from the null values of products of rows or columns of orthogonal matrices.

The torque must be expressed in terms of the variables used in the differential equations (p_i, q_i), which refer to the orbit system of coordinates and where $p_i = \sin i_i \sin\Omega_i$, $q_i = \sin i_i \cos\Omega_i$. The variables ψ_i will be rapidly varying because of the rotations. We will average over the ψ_i to retain only the slowly varying components. The core and mantle systems of coordinates are oriented relative to the orbit system through the Euler angles Ω_i, i_i, ψ_i with the orthogonal transformation $\mathbf{A}$ given by Goldstein (1980, p. 147) with rows (A_{11}, A_{12}, A_{13}), $(A_{21}, ...)$, $(A_{31}, ...)$. The X, Y, Z orbit system has the X axis along the

ascending node of the orbit on the Laplace plane on which the orbit precesses with a nearly constant inclination at nearly a constant rate with a $\sim 300,000$ year period. The Z axis is normal to the orbit (XY) plane. $\mathbf{I}, \mathbf{J}, \mathbf{K}$ are unit vectors along the X, Y, Z axes. From Goldstein (1980), $(X_m, Y_m, Z_m) = \mathbf{A}_m^{-1}(x_m, y_m, z_m)$, so that, for example, $\mathbf{i}_m = (1, 0, 0)$ in the mantle frame has components $A_{m11}\mathbf{I} + A_{m12}\mathbf{J} + A_{m13}\mathbf{K}$ in the orbit frame, with similar expressions for $\mathbf{j}_m$ and $\mathbf{k}_m$ in terms of the A_{mij}. The unit vectors along the mantle principal axes $(\mathbf{i}_m, \mathbf{j}_m, \mathbf{k}_m)$ are thus expressed in the orbit system in terms of the appropriate Euler angles. A similar set of expressions involving the components of the transformation $\mathbf{A}_s$ orienting the inner core relative to the orbit plane in terms of the Euler angles Ω_s, i_s, ψ_s yields the components of $\mathbf{i}_s, \mathbf{j}_s, \mathbf{k}_s$ in the orbit system.

From the definition of the transformation with components ℓ_i, m_i, n_i orienting the inner core relative to the mantle, we can deduce that $\ell_1 = \mathbf{i}_s \cdot \mathbf{i}_m$, $\ell_2 = \mathbf{j}_s \cdot \mathbf{i}_m$, $\ell_3 = \mathbf{k}_s \cdot \mathbf{i}_m$, $m_1 = \mathbf{i}_s \cdot \mathbf{j}_m$, $m_2 = \mathbf{j}_s \cdot \mathbf{j}_m$, $m_3 = \mathbf{k}_s \cdot \mathbf{j}_m$, $n_1 = \mathbf{i}_s \cdot \mathbf{k}_m$, $n_2 = \mathbf{j}_s \cdot \mathbf{k}_m$, $n_3 = \mathbf{k}_s \cdot \mathbf{k}_m$. Since the components of all the unit vectors are known in the orbit system of coordinates in terms of the respective sets of Euler angles, the torque on the inner core from the asymmetric mantle is known in terms of the same coordinates. Finally, expressing $\mathbf{i}_m, \mathbf{j}_m, \mathbf{k}_m$ in terms of their components along $\mathbf{I}, \mathbf{J}, \mathbf{K}$ and collecting terms for each of the latter unit vectors yields the components of $\mathbf{T}^s_{mantlegrav}$ in the orbit system in terms of the respective Euler angles.

The many terms in $\mathbf{T}^s_{mantlegrav}$ are expanded into products of circular functions whose arguments are single Euler angles orienting the mantle and inner core relative to the orbit system. This expansion is averaged over the Mercury day to eliminate the high-frequency terms. We will consider only small starting values of the Euler angles i_m and i_s (obliquities) close to the current obliquity of the mantle of ~ 2 arcmin (Margot et al. 2007, 2012). As the obliquities will remain small throughout the calculation, we keep only those terms in the sum of products of the circular functions with single angles as arguments representing $\mathbf{T}^s_{mantlegrav}$ that are first order in i_c, i_m. (The thousands of lines involved in this exercise were handled with the Mathematica software package, but considerable hand editing of the files was necessary in order to use editorial macros to efficiently eliminate the higher-order terms.) Mercury's 3:2 spin-orbit resonance requires $\dot{\psi}_m = 1.5n + \dot{\gamma}_m$ and $\dot{\psi}_s = 1.5n + \dot{\gamma}_s$, where n is the orbital mean motion and $\dot{\gamma}_m$ and $\dot{\gamma}_s$ allow for small deviations of the rotation rates from the resonant values. The stability of the resonance requires the axis of minimum moment of inertia of Mercury to be nearly aligned with the direction to the Sun when Mercury is at perihelion. A slight displacement from this condition will cause a free libration in longitude about this position that will be damped by dissipation. Because of the small obliquities

assumed, we can write

$$\begin{aligned}\psi_m &= 1.5M + \omega - \Omega_m + \gamma_m \\ \psi_s &= 1.5M + \omega - \Omega_s + \gamma_s,\end{aligned} \tag{13}$$

which follows from inspection of Fig. 1, where ω is the argument of perihelion, M is the mean anomaly, and the Euler angles Ω_m and Ω_s are the longitudes of the ascending nodes of the equator planes of the mantle and inner core, respectively, measured from the X axis in the orbit plane. With ψ_m and ψ_s replaced by the expressions in Eq. (13), we perform the operation

$$\langle \mathbf{T}^s_{mantlegrav} \rangle = \frac{1}{4\pi} \int_0^{4\pi} \mathbf{T}^s_{mantlegrav} dM, \tag{14}$$

to obtain the averaged torque on the inner core due to the gravitational potential of the asymmetric mantle–crust. In the average, the only quantity to survive from the expressions for ψ_m and ψ_s is $2\gamma_m - 2\gamma_s$, always in this combination.

$\langle \mathbf{T}^s_{mantlegrav} \rangle$ contains circular functions with arguments containing i_m, Ω_m, i_s, Ω_s in addition to circular functions with argument $2\gamma_m - 2\gamma_s$. The circular functions involving the Euler angles are expressed in terms of p_m, q_m, p_s, q_s. $\langle \mathbf{T}^s_{mantlegrav} \rangle$ is thereby expressed in terms of the variables in the differential equations, where $d\psi_i/dt$ is replaced by $d\dot{\gamma}_i/dt$. The torque on the mantle due to the asymmetric inner core is $-\langle \mathbf{T}^s_{mantlegrav} \rangle$. Simplification of many lines leads to the expression for $\langle \mathbf{T}^s_{mantlegrav} \rangle$ to be used in the equations of motion:

$$\begin{aligned}\langle T^s_{mantlegrav} \rangle_X &= \frac{16}{75}\pi^2 G R_s^5 (\rho_s - \rho_f)\{[4K_a\epsilon_s + K_b\xi_s \cos(2\gamma_m - 2\gamma_s)](q_m - q_s) \\ &\quad + \xi_s K_b (p_m + p_s)\sin(2\gamma_m - 2\gamma_s)\}, \\ \langle T^s_{mantlegrav} \rangle_Y &= \frac{16}{75}\pi^2 G R_s^5 (\rho_s - \rho_f)\{[4K_a\epsilon_s + K_b\xi_s \cos(2\gamma_m - 2\gamma_s)](p_m - p_s) \\ &\quad - \xi_s K_b (q_m + q_s)\sin(2\gamma_m - 2\gamma_s)\}, \\ \langle T^s_{mantlegrav} \rangle_Z &= \frac{16}{75}\pi^2 G R_s^5 (\rho_s - \rho_f)\{[-4K_a\epsilon_s + K_b\xi_s \cos(2\gamma_m - 2\gamma_s)](p_s q_m - p_m q_s) \\ &\quad + \xi_s [K_b(p_m p_s + q_m q_s) + 2K_b]\sin(2\gamma_m - 2\gamma_s)\},\end{aligned} \tag{15}$$

where

$$\begin{aligned}K_a &= \epsilon_m \rho_m + \epsilon_f(\rho_f - \rho_m), \\ K_b &= \xi_m \rho_m + \xi_f(\rho_f - \rho_m),\end{aligned}$$

Eqs. (15) are accurate to first order in i_m, i_c. To be consistent with this assertion, the products of the qs and ps should also be ignored in $\langle T^s_{mantlegrav} \rangle_Z$.

2.3. Viscous torques

The viscous torque provides the necessary dissipation to bring the system to equilibrium from initial conditions that are close to the equilibrium but otherwise arbitrary. The viscous torque at the CMB and ICB is assumed to be simply proportional to the difference in the vector angular velocities. This assumption is consistent with the fluid core rotating as a rigid body (Poincaré 1910).

$$\begin{aligned}
\langle \mathbf{T}^m_{viscous} \rangle &= -\beta_1(\dot{\boldsymbol{\psi}}_{\boldsymbol{m}} - \dot{\boldsymbol{\psi}}_{\boldsymbol{f}}), \\
\langle \mathbf{T}^s_{viscous} \rangle &= -\beta_2(\dot{\boldsymbol{\psi}}_{\boldsymbol{s}} - \dot{\boldsymbol{\psi}}_{\boldsymbol{f}}), \\
\langle \mathbf{T}^f_{viscous} \rangle &= -\mathbf{T}^m_{viscous} - \mathbf{T}^s_{viscous}
\end{aligned} \tag{16}$$

are the viscous torques on the mantle, solid inner core, and fluid outer core, respectively, where the viscous torques are intrinsically averaged since they do not contain the mean anomaly and where

$$\begin{aligned}
\beta_1 &= \frac{\nu}{R_f^2} \frac{(C_m + C_c)C_f}{C_m + C_c + C_f}, \\
\beta_2 &= \frac{\nu}{R_s^2} \frac{C_s C_f}{C_s + C_f}
\end{aligned} \tag{17}$$

are the coefficients for the CMB and the ICB, respectively. In Eqs (17), ν is the kinematic viscosity of the core fluid and the Cs are polar moments of inertia. These forms are found by equating the time constant for the decay of a differential angular velocity as determined from Eqs. (16) with the viscous time scale R^2/ν (*e.g.*, Paper 1).

With $\dot{\boldsymbol{\psi}}_{\boldsymbol{m}} = \dot{\psi}_m \mathbf{k}_m = \dot{\psi}_m[p_m \mathbf{I} - q_m \mathbf{J} + \sqrt{1 - p_m^2 - q_m^2}\mathbf{K}]$ and with a similar expression for $\dot{\boldsymbol{\psi}}_{\boldsymbol{f}}$, we can write for the viscous torque on the mantle

$$\begin{aligned}
\langle T^m_{viscous} \rangle_X &= -\beta_1(p_m \dot{\psi}_m - p_f \dot{\psi}_f), \\
\langle T^m_{viscous} \rangle_Y &= -\beta_1(-q_m \dot{\psi}_m + q_f \dot{\psi}_f), \\
\langle T^m_{viscous} \rangle_Z &= -\beta_1(\dot{\psi}_m \sqrt{1 - p_m^2 - q_m^2} - \dot{\psi}_f \sqrt{1 - p_f^2 - q_f^2}),
\end{aligned} \tag{18}$$

which is now expressed in terms of the variables in the variational equations. Similar expressions apply for the viscous torque on the inner core with superscripts and subscripts m replaced by s.

2.4. Pressure torques

From Appendix A, the pressure torques on the mantle–crust at the CMB and on the inner core at the ICB are

$$\begin{aligned} \mathbf{T}^m_{pressure} &= \iint_{CMB} \mathbf{r} \times \mathbf{n} P dS, \\ \mathbf{T}^s_{pressure} &= -\iint_{ICB} \mathbf{r} \times \mathbf{n} P dS, \end{aligned} \tag{19}$$

where $\mathbf{n}$ is the normal to the surface in the positive radial direction. The surface integrals can be expressed in terms of an integral over the volume of the fluid core (Appendix A)

$$\iiint_V \mathbf{r} \times \nabla P dV,$$

where $\nabla P = -\rho_f(\partial \mathbf{v}/\partial t + (\mathbf{v} \cdot \nabla)\mathbf{v} + \nabla\Phi)$ separates the contributions to the pressure torque into two parts—one depending on the fluid motion and the other on the gravitational potential Φ at the point. We have already accounted for the contributions of Φ to the pressure torque at the CMB by including the thin layer of fluid core material that is outside the largest sphere that fits inside the CMB with J_2 and C_{22} of the mantle, and at the ICB by substituting $\rho_s - \rho_f$ for ρ_s in the expression for the ordinary gravitational torque on the solid inner core (Appendix A). We will assume a steady state, so $\partial \mathbf{v}/\partial t = 0$, which leaves the contribution from $(\mathbf{v} \cdot \nabla)\mathbf{v}$ to be determined.

From the discussion at the beginning of Section 2.2, we can represent an axially symmetric ellipsoidal CMB by $x'^2 + y'^2 + f_{\epsilon_f} z'^2 = a^2$, where x', y', z' are non-rotating coordinates along principal axes defining the CMB and $f_{\epsilon_f} = 1 + 2\epsilon_f$ to first order in ϵ_f. We choose axial symmetry here to take advantage of developments applied to the Earth's interior by Melchior (1986). The normal to this ellipsoidal surface is $\mathbf{n} = \nabla a^2/|\nabla a^2| = (x'\mathbf{i}' + y'\mathbf{j}' + f_{\epsilon_f} z'\mathbf{k}')/\sqrt{x'^2 + y'^2 + f^2_{\epsilon_f} z'^2}$. In Paper 1 we followed Melchior (1986, p. 218–222) by representing the velocity of the fluid in the core as a perturbation of rigid body motion:

$$\mathbf{v} = (\dot\psi_{fy'} z' - \dot\psi_{fz'} y')\mathbf{i}' + (\dot\psi_{fz'} x' - \dot\psi_{fx'} z')\mathbf{j}' + \frac{(\dot\psi_{fx'} y' - \dot\psi_{fy'} x')}{f_{\epsilon_f}}\mathbf{k}', \tag{20}$$

which satisfies the boundary condition of $\mathbf{v} \cdot \mathbf{n} = 0$. In Eq. (20) $\dot\psi_{fi}$ are the components of fluid velocity in the principal axis $x'y'z'$ system that does not rotate with the fluid core. In Paper 1, Eq. (20) is used to determine $(\mathbf{v} \cdot \nabla)\mathbf{v}$, and the scalar representing the pressure P_{CMB} is determined such that ∇P_{CMB} has the components of $-(\rho_f \mathbf{v} \cdot \nabla)\mathbf{v}$. Integration of the

first of Eqs. (19) with this expression for P_{CMB} yields for this part of the pressure torque on the mantle,

$$\mathbf{T}^{(m)(\mathbf{v}\cdot\nabla)\mathbf{v}}_{pressure} = -\frac{8\pi}{15}\rho_f\epsilon_f R_f^5\dot{\psi}_{fz'}(\dot{\psi}_{fy'}\mathbf{i}' - \dot{\psi}_{fx'}\mathbf{j}'). \tag{21}$$

The form of the fluid velocity at the ICB is identical to that in Eq. (20) for the CMB except now the coordinates refer to the principal axes of the solid inner core, and the components of the angular velocities are relative to these axes. The pressure

$$P = -\rho_f\left[\frac{x'y'\dot{\psi}_{fy'}\dot{\psi}_{fx'}}{f_{\epsilon_s}} + z'x'\dot{\psi}_{fz'}\dot{\psi}_{fx'} + z'y'\dot{\psi}_{fz'}\dot{\psi}_{fy'} - (x'^2+z'^2)\frac{\dot{\psi}^2_{fy'}}{2f_{\epsilon_s}} - (x'^2+y'^2)\frac{\dot{\psi}^2_{fz'}}{2} - (y'^2+z'^2)\frac{\dot{\psi}^2_{fx'}}{2f_{\epsilon_s}}\right] \tag{22}$$

produces the components of that part of ∇P that comes from $(\mathbf{v}\cdot\nabla)\mathbf{v}$ except for f_{ϵ_s} missing in two terms in the denominator of the $\mathbf{k}'$ component. But

$$\mathbf{r}\times\mathbf{n} = \frac{f_{\epsilon_s}-1}{R_s}z'(y'\mathbf{i}' - x'\mathbf{j}'), \tag{23}$$

contains the factor ϵ_s, so f_{ϵ_s} in the denominator becomes 1 in the numerator of Eq. (19) to first order in ϵ_s. With Cartesian coordinates changed to spherical surface harmonics, integration of the second of Eq. (19) yields

$$\mathbf{T}^{(s)(\mathbf{v}\cdot\nabla)\mathbf{v}}_{pressure} = \frac{8\pi}{15}\rho_f\epsilon_s R_s^5\dot{\psi}_{fz'}(\dot{\psi}_{fy'}\mathbf{i}' - \dot{\psi}_{fx'}\mathbf{j}'), \tag{24}$$

for the torque on the inner core due to the $(\mathbf{v}\cdot\nabla)\mathbf{v}$ part of ∇P. Note that this is the same form as Eq. (21) except the coordinates refer to the solid inner core principal axis system and the sign is reversed.

Eqs. (21) and (24) must be written in terms of the variables in Eq. (1). Since the bracketed term in these two equations is $-\mathbf{k}'\times\dot{\boldsymbol{\psi}}_{\boldsymbol{f}}$, the choice of orientation of $\mathbf{i}'$ and $\mathbf{j}'$ in the respective equator planes is arbitrary. We chose to orient $\mathbf{i}'$ along the ascending node of the equator plane on the orbit plane such that for the inner core

$$\begin{aligned}\mathbf{i}' &= \frac{q_s}{\sqrt{p_s^2+q_s^2}}\mathbf{I} + \frac{p_s}{\sqrt{p_s^2+q_s^2}}\mathbf{J}\\ \mathbf{j}' &= -\frac{p_s\sqrt{1-p_s^2-q_s^2}}{\sqrt{p_s^2+q_s^2}}\mathbf{I} + \frac{q_s\sqrt{1-p_s^2-q_s^2}}{\sqrt{p_s^2+q_s^2}}\mathbf{J} + \sqrt{p_s^2+q_s^2}\mathbf{K}\end{aligned} \tag{25}$$

With $\mathbf{k}' = p_s\mathbf{I} - q_s\mathbf{J} + \sqrt{1-p_s^2-q_s^2}\mathbf{K}$ and a similar expression for $\mathbf{k}'_f$ and with $\dot{\psi}_{fz'} =$

$\dot{\psi}_f \mathbf{k'}_f \cdot \mathbf{k'}$, $\dot{\psi}_{fx'} = \dot{\psi}_f \mathbf{k'}_f \cdot \mathbf{i'}$, and $\dot{\psi}_{fy'} = \dot{\psi}_f \mathbf{k'}_f \cdot \mathbf{j'}$, we can write

$$\begin{aligned}
\dot{\psi}_{fx'} &= \dot{\psi}_f \left(\frac{p_f q_s}{\sqrt{p_s^2 + q_s^2}} - \frac{q_f p_s}{\sqrt{p_s^2 + q_s^2}} \right) \\
\dot{\psi}_{fy'} &= \dot{\psi}_f \left(-\frac{p_f p_s \sqrt{1 - p_s^2 - q_s^2}}{\sqrt{p_s^2 + q_s^2}} - \frac{q_f q_s \sqrt{1 - p_s^2 - q_s^2}}{\sqrt{p_s^2 + q_s^2}} + \sqrt{(1 - p_f^2 - q_f^2)(p_s^2 + q_s^2)} \right) \\
\dot{\psi}_{fz'} &= \dot{\psi}_f \left[p_f p_s + q_f q_s + \sqrt{(1 - p_f^2 + q_f^2)(1 - p_s^2 - q_s^2)} \right] . \qquad (26)
\end{aligned}$$

Substitution of Eqs. (26) and (25) into Eq. (24) yields $\mathbf{T}^{(m)(\mathbf{v}\cdot\nabla)\mathbf{v}}_{pressure}$ in terms of the variables of Eq. (1). Eqs. (25) and (26) also apply to the conversion of Eq. (21) to the proper variables in the equations of variation by changing the subscripts s to m.

2.5. Torque on the fluid core

The fluid core is subject to the negatives of the pressure torques on the mantle at the CMB and on the inner core at the ICB. The potential part of the pressure torque on the mantle is equivalent to the gravitational torque on the thin layer of core fluid outside the largest sphere that fits inside the CMB. The negative of this torque, part of the pressure torque on the fluid core, exactly cancels the direct gravitational torque on this part of the core. Similarly, the negative of the pressure torque exerted on the inner core is a positive torque on a thin sheet of material of fluid core density outside the largest sphere that fits inside the ICB. This is exactly canceled by the direct negative torque on the fluid core from the absence of that material in the same thin sheet. The gravitational torque on the fluid core thereby completely disappears, and the only torques remaining are the pressure torques from the $(\mathbf{v} \cdot \nabla)\mathbf{v}$ source and the negative of the viscous torques on the CMB and the ICB.

$$\mathbf{T}_f = -\mathbf{T}^{(m)(\mathbf{v}\cdot\nabla)\mathbf{v}}_{pressure} - \mathbf{T}^{(s)(\mathbf{v}\cdot\nabla)\mathbf{v}}_{pressure} - \mathbf{T}^{m}_{viscous} - \mathbf{T}^{s}_{viscous} \qquad (27)$$

All the necessary torques on each of the distinct layers in Mercury are now collected. We have only to insert these torques into Eqs. (1) and integrate the system of nine equations from initial conditions close to the final state until an equilibrium configuration is reached.

The torques on each layer are summarized below.

$$\begin{aligned}
\langle \mathbf{T}_m \rangle &= \langle \mathbf{T}^{m}_{solar} \rangle - \langle \mathbf{T}^{s}_{mantlegrav} \rangle + \langle \mathbf{T}^{(m)(\mathbf{v}\cdot\nabla)\mathbf{v}}_{pressure} \rangle + \langle \mathbf{T}^{m}_{viscous} \rangle \\
\langle \mathbf{T}_f \rangle &= -\langle \mathbf{T}^{(m)(\mathbf{v}\cdot\nabla)\mathbf{v}}_{pressure} \rangle - \langle \mathbf{T}^{(s)(\mathbf{v}\cdot\nabla)\mathbf{v}}_{pressure} \rangle - \langle \mathbf{T}^{m}_{viscous} \rangle - \langle \mathbf{T}^{s}_{viscous} \rangle \\
\langle \mathbf{T}_s \rangle &= \langle \mathbf{T}^{s}_{solar} \rangle + \langle \mathbf{T}^{s}_{mantlegrav} \rangle + \langle \mathbf{T}^{(s)(\mathbf{v}\cdot\nabla)\mathbf{v}}_{pressure} \rangle + \langle \mathbf{T}^{s}_{viscous} \rangle \qquad (28)
\end{aligned}$$

Other formulations for gravitational and pressure torques between inner core, outer core, and mantle have been given by Szeto and Xu (1997); Baland and van Hoolst (2010); Baland et al. (2011).

3. Results

The expressions for $\langle T_m \rangle$, $\langle T_f \rangle$, and $\langle T_s \rangle$ in Eqs. (28) are substituted into the first of Eqs. (2) with the appropriate subscripts, and the resulting expressions for the components of $\mathbf{N}_m$, $\mathbf{N}_f$, and $\mathbf{N}_s$ are substituted into the three sets of equations of the form of Eqs. (1). The set of nine equations are solved numerically with a Bulirsh-Stoer algorithm with initial conditions that are close to the final equilibrium state to sustain the approximations used to derive the equations but are otherwise arbitrary. Since $\dot{\psi}_i = 1.5n + \dot{\gamma}_i$, $d\dot{\gamma}_i/dt$ replaces $d\dot{\psi}_i/dt$ in Eqs. (1). The initial conditions for all the calculations are as follows: $i_m = 0.01°$, $i_f = 0.0°$, $i_s = 0.01°$, $\Omega_m = 0.0°$, $\Omega_f = 180°$, $\Omega_s = 90°$, $\gamma_m = 0.01°$, $\dot{\gamma}_m = 0.0001°$/day, $\dot{\gamma}_f = 0.0001°$/day, $\gamma_s = 0.0°$, $\dot{\gamma}_s = 0.0001°$/day. The equations are integrated until there is no further change in the spin positions to 8 significant figures.

A typical damping of the spin angular velocities from the initial conditions for $R_s = 0.6R_c$ for viscosity $\nu = 7.15 \times 10^3\,\mathrm{cm}^2/\mathrm{s}$ and $\rho_s = 8.0\,\mathrm{g/cm}^3$ is shown in Fig. 3. The value of the viscosity determines the rate of approach to the equilibrium rotation rates. The inner core and the mantle both progress to the exact resonance with $\dot{\gamma}_m$ and $\dot{\gamma}_s$ going to zero. This equilibrium is a consequence of the axial asymmetry of both the mantle–crust and the solid inner core. Both $\dot{\psi}_m$ and $\dot{\psi}_s$ must necessarily librate about the resonant $1.5n$, which librations damp to zero amplitude as shown. Interestingly, the fluid outer core ends up with an angular velocity slightly less than the resonant value. For the case of $R_s = 0.6R_c$ shown, the fluid core is rotating $8.714 \times 10^{-7}\,°$/day slower than the mantle and inner core. The fluid core makes one revolution relative to the mantle in 1.13×10^6 yr. This period corresponds to a differential motion of 3.1 cm/day at the equator of the CMB. The relative rotation of the fluid core increases as the inner core shrinks, with one revolution relative to the mantle and inner core in 3.47×10^5 yr for $R_s = 0.4R_c$ (10.1 cm/day) and 3.14×10^5 yr for $R_s = 0.3R_c$ (11.2 cm/day) for the case with $\rho_s = 8.0\,\mathrm{g/cm}^3$. Recall that only the pressure torques from the fluid motion and viscous torques at the CMB and the ICB act on the fluid core, where the relative rotation of the fluid core is essentially the same for the two values of viscosity for $R_s = 0.6R_c$, which indicates that the viscous torques are relatively unimportant in determining the final state.

An illustration of a typical evolutionary trajectory for the projection of the unit mantle

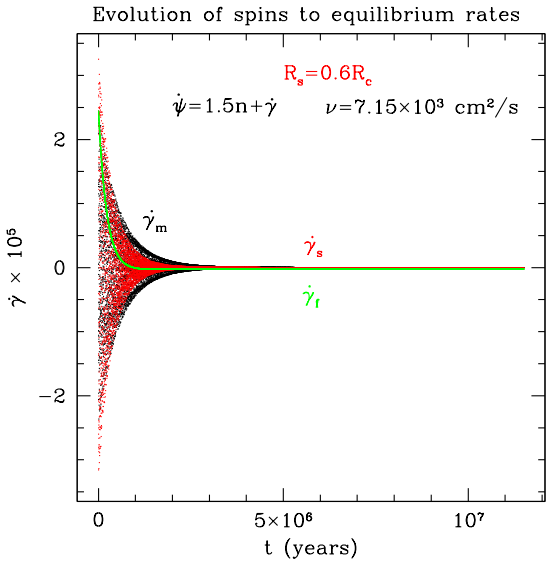

Fig. 3.— An example of damping of the mantle–crust, solid inner core, and fluid outer core to their final equilibrium rotation rates for $R_s = 0.6R_c$. The mantle and inner core end up precisely in the spin-orbit resonance, but the fluid core rotates at a slightly slower rate as described in the text.

spin vector onto the orbit plane is shown Fig. 4. The decay of the spin toward equilibrium is fast (5.9×10^6 yr) because of the artificially high viscosity of $\nu = 2.26 \times 10^5\,\mathrm{cm}^2/\mathrm{s}$. The left panel shows the evolution from the initial conditions, and the right panel shows the final approach to the equilibrium circle traced by the spin axis in the steady state. The position of the equilibrium depends on the argument of perihelion of Mercury's orbit, and the projection of the spin vector makes two circuits of the circle per period of perihelion precession. The radius of the circle is 0.87 arcsec, and the displacement of the center of the circle from the nominal Cassini-state position marked by the large X is 1.38 arcsec, both considerably less than the current 5 arcsec uncertainty in the spin axis position (Margot et al. 2012). (The theoretical position of the Cassini state is that determined for a rigid planet that depends on J_2, C_{22}, and C/mR_c^2 (e.g., Peale 1969, 1974). The same position results for a planet with a fluid core but no solid inner core (Peale et al. 2014). The measured values of the obliquity, J_2, and C_{22} are, in fact, used together with the obliquity to determine C/mR_c^2.) The equilibrium circle is reached in about 1.07×10^8 yr if the viscosity is reduced to $7.15 \times 10^3\,\mathrm{cm}^2/\mathrm{s}$. The more complicated approach to equilibrium for the lower viscosity is shown in Fig. 5. Here the trajectory oscillates about the equilibrium circle and gradually becomes more confined near

the curve as the dissipation continues. The white trajectory in the figure marks the near approach to the equilibrium circle. There is a 0.05 arcsec displacement of the equilibrium circle toward the fourth quadrant in the right panel of Fig. 4 because of the higher viscous dissipation. Such displacement is almost undetectable in Fig. 5 with the lower viscosity.

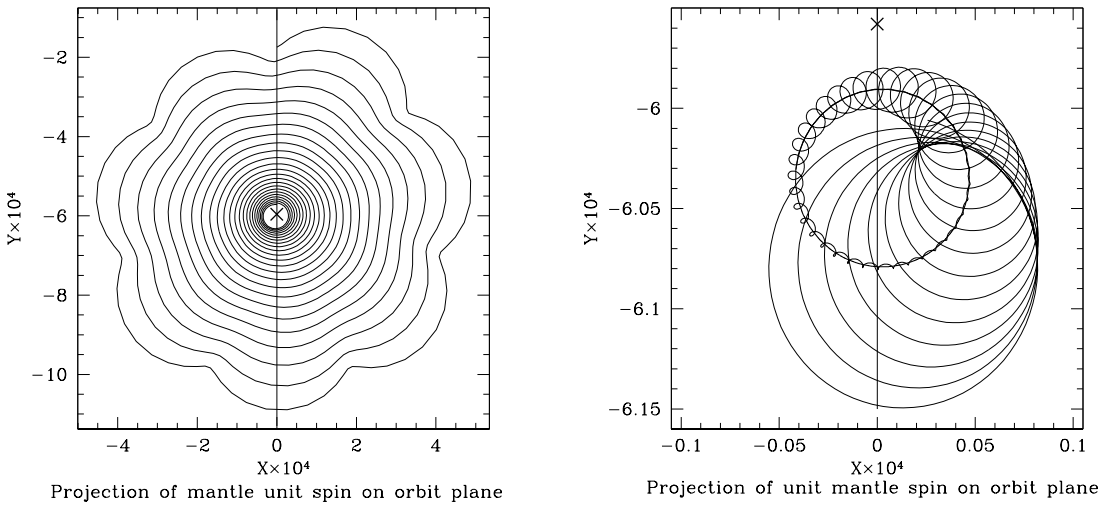

Fig. 4.— Evolution of the projection onto the orbit plane of the unit spin vector of the mantle for inner core radius $R_s = 0.3R_c$ and density $\rho_s = 8.0$ g/cm^3 as an example of rapid damping for a viscosity $\nu = 2.26 \times 10^5$ cm^2/s. The left panel is the initial spiral toward the equilibrium position. The right panel shows the final decay to the limiting circle that is traced because of the advance of the orbit perihelion. The large X is the location of the nominal Cassini state. Since the angles are small, the coordinates represent radians. (6×10^{-4} rad = 2.06 arcmin.)

The location of the equilibrium spins as a function of inner core size R_s for $\rho_s = 8.0$ g/cm^3 is shown in Fig. 6 (left panel). The inner core spin always has the largest obliquity and is represented by the lower of the two points marked for each R_s in the Figure. The other points in each pair are the fluid core positions. The large X symbols denote the projection of the Cassini state onto the orbit plane and the position of the fluid core spin for $R_s = 0$. The mantle–crust spins are grouped near the projection of the Cassini state. Only the mantle–crust spin position for $R_s/R_c = 0.6$ is indicated with an arrow. The other mantle–crust equilibrium spins for smaller R_s lie above that for $R_s/R_c = 0.6$ as shown in the higher-resolution figure in the right panel.

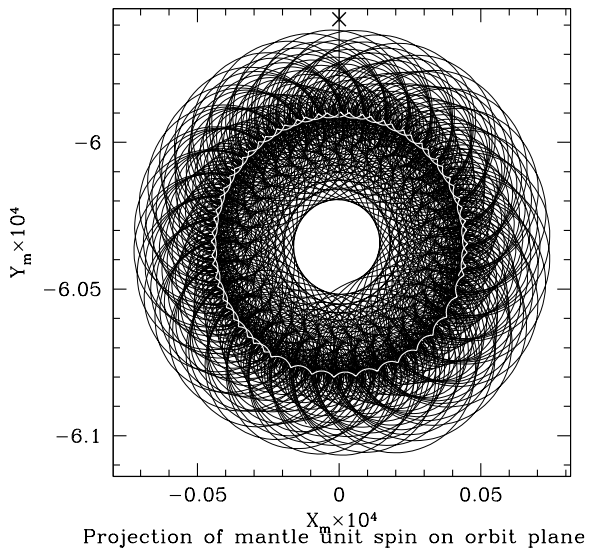

Fig. 5.— Final damping of the projection of the unit mantle spin for the same parameters as those in Fig. 4 except that the viscosity is reduced to $7.15 \times 10^3\,\mathrm{cm}^2/\mathrm{s}$. The large X marks the position of the nominal Cassini state. The white superposed curve is approaching the same limiting circle seen in the right panel of Fig. 4.

The displacement of the mantle–crust spin axis from the Cassini state increases as R_s increases. For each value of R_s and density ρ_s, Eqs. (1) are integrated until there is no longer any change in the configuration to 8 significant figures. The equilibria of the spin positions so attained are characterized by the small circles of less than 1 arcsec radius traced by the projections of the unit spin vectors onto the orbit plane shown in the right panel of Fig. 4 and in Fig. 5. The final equilibrium states for the spins of all the Mercury parts for five values of R_s are illustrated in the left panel in Fig. 6, again as projections of the unit spin vectors onto the orbit plane. The large X symbols mark the nominal Cassini state for the mantle and the corresponding position of the fluid core for $R_s = 0$. The small ellipse bounds the one-standard-deviation uncertainty in the observed location of the mantle spin (Margot et al. 2012). The equilibrium location of the mantle spin for $R_s = 0.3R_c$ is within the observational uncertainty of the mantle spin position, and the circles traced by projections of the unit spins of the fluid outer core and solid inner core for this R_s are almost coincident and are similarly close to the fluid core spin for $R_s = 0$. But for $R_s = 0.4R$, the mantle spin is displaced to a higher obliquity that is outside the one-standard-deviation uncertainty of the observed spin location. This displacement increases as the size of the inner core is

increased, with equilibria for additional values of R_s shown in the right panel of Fig. 6.

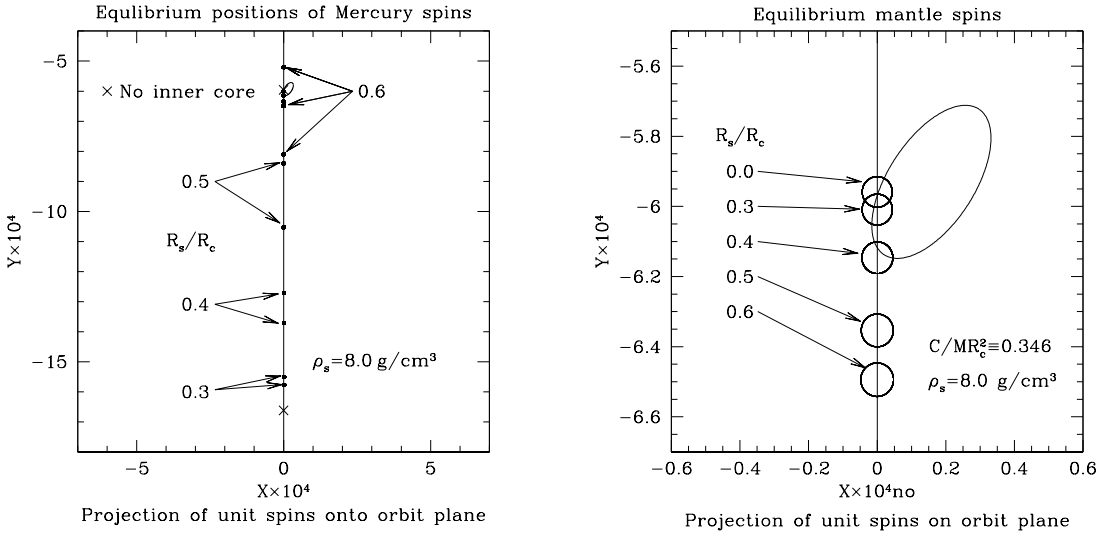

Fig. 6.— (Left) Distribution of equilibrium spins as a function of the inner core size for $\rho_s = 8.0$ g/cm^3. The large upper and lower X symbols mark the Cassini state projection and the projection of the fluid core spin for $R_s = 0$, respectively. The inner core obliquity is always greater than that of the fluid core, and it is represented by the lower point associated with each R_s. The mantle spins are grouped close to the nominal Cassini state, moving farther away to higher obliquities as R_s increases. For $R_s/R_c = 0.6$ a third arrow shows the mantle spin position, below the uncertainty ellipse. (Right) A high-resolution figure shows the distribution of mantle spins explicitly. Reminder: R_c is the radius of the planet.

For the viscosity $\nu = 7.15 \times 10^3\,\mathrm{cm}^2/\mathrm{s}$ (and smaller viscosities) all the spin equilibria are nearly centered on the plane defined by the orbit and Laplace plane normals, where the Cassini state of the mantle is also located. The inner and outer cores end up in their own Cassini states. The obliquities are maintained during the precession.

The equivalent of Fig. 6 is shown in Fig. 8 for inner core densities of 9.3 and 10.0 g/cm^3. All the models are summarized in Table 1.

4. Discussion

We reduced the 16 unknowns to 10 by specifying ρ_s, R_s, ρ_c, R_m and by using the measured values of ϵ_c and ξ_c. With the six known quantities m, R_c, C/mR_c^2, $(C_m+C_c)/C$, J_2, C_{22} and four equations for the equipotential surfaces, the 10 equations allowed the solution for the 10 unknowns, and we could characterize Mercury for each of the assumed inner core sizes and densities. Inherent in all the solutions is the use of C/mR_c^2 determined from the obliquity of the mantle spin and coefficients J_2 and C_{22}. Therein lies the clue to understanding the meaning of the displacement of the spin axis away from the Cassini state by the addition of the ellipsoidal solid inner core.

It appears that an inner core radius $R_s \gtrsim 0.35R_c$ would drag the mantle spin away from the Cassini state by an amount that exceeds the current observational uncertainty of ~ 5 arcsec. The fact that the torque from the inner core can change the position of the spin means that the classical determination of the Cassini state position is not complete. We must add the torque from the inner core on the mantle to the external torque from the Sun in evaluating the Cassini state position. This result also means that the determination of C/mR_c^2 will depend on the size and shape of the inner core and that it will thereby be more uncertain than heretofore assumed. Peale et al. (2014) found that as the dissipative core–mantle torques weakened, the mantle spin approached a Cassini state with a lower obliquity. The weakened dissipative torque means that the mantle is less affected by the fluid core, and the Cassini state approached is that for the smaller moment of inertia of the mantle alone. This result suggests that a smaller moment of inertia can compensate for the gravitational torque from the solid inner core and bring the mantle spin back to its observed position in the presence of the inner core. We found earlier that dissipative torques displaced the spin from the Cassini state by amounts that exceeded observational uncertainties, but that pressure torques between a liquid core and solid mantle restored the mantle spin to the nominal Cassini state position (Peale et al. 2014). Here the introduction of an ellipsoidal solid inner core overrides this pressure effect and moves the mantle spin away from the Cassini state that corresponds to there being no solid inner core. The cause of this displacement is entirely due to the gravitational torque between the solid inner core and the mantle. If this torque is set to zero with all other torques remaining, the mantle spin goes back to the nominal Cassini state.

A procedure for ascertaining C/mR_c^2 as a function of the inner core size, where the latter is assumed to be in hydrostatic equilibrium in the internal gravitational field of the mantle, is as follows: We choose an inner core size and density, then guess the value of $C/mR_c^2 < 0.346$ that will lead to an obliquity within the observational uncertainty. The smaller C/mR_c^2 will

lead to a larger $(C_m + C_c)/C$ as determined by the equation

$$\left(\frac{C_m + C_c}{B - A}\right)\left(\frac{B - A}{mR_c^2}\right)\left(\frac{mR_c^2}{C}\right) = \frac{C_m + C_c}{C}, \tag{29}$$

where the first factor follows from the amplitude of the physical libration in longitude (Margot et al. 2012), and the second from the MESSENGER determined value of C_{22} (Smith et al. 2012; Mazarico et al. 2014). C/mR_c^2, $(C_m + C_c)/C$, and m are used in Eq. (41) of Appendix A of Peale et al. (2014) to determine ρ_m, ρ_f, and R_f. The procedure of Appendix A of Peale et al. (2014) is then used to determine the mean polar and equatorial ellipticities of the ICB, CMB, and mantle surface that are consistent with their respective contributions to the known values of J_2 and C_{22} and consistent with hydrostatic equilibrium of the CMB and the ICB. This procedure allows the several torques to be determined for use in Eqs. (1). Starting with initial conditions close to the equilibrium values of the spin positions, the system is then evolved to equilibrium through the numerical solution of Eqs. (1), where the viscous dissipation takes the spin vectors to the new positions appropriate to the chosen values of R_s, ρ_s, and C/mR_c^2. If the obliquity of the mantle is outside the observational uncertainty, C/mR_c^2 is adjusted in a direction that reduces or increases the obliquity as necessary, and the entire procedure is repeated.

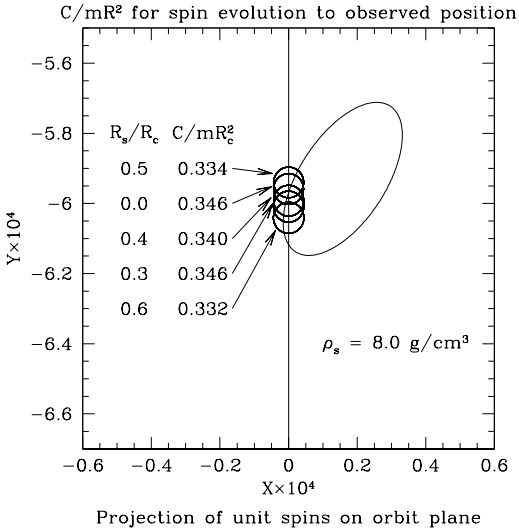

Fig. 7.— Positions of the mantle–crust spins adjusted by reducing $C = mR_c^2$ to the indicated values for $\rho_s = 8$ g/cm^3. All the spins are now within the uncertainty of the observed pole position. Reminder: R_c is the radius of the planet.

The result of this exercise is shown in Fig. 7 for $\rho_s = 8.0\,\mathrm{g/cm^3}$, where the moved

positions of the mantle spins are shown along with the necessary value of C/mR_c^2 to bring the spin within the observational uncertainty of the mantle spin position as a function of R_s. The changes required in C/mR_c^2 are significant and increase with R_s. We do not know the density of the inner core. So to bridge a possible range of inner core densities, we have performed a similar exercise for inner core densities of 9.3 and 10.0 g/cm^3, for which the results are shown in Fig. 8. The increased inner core densities seem to require even smaller

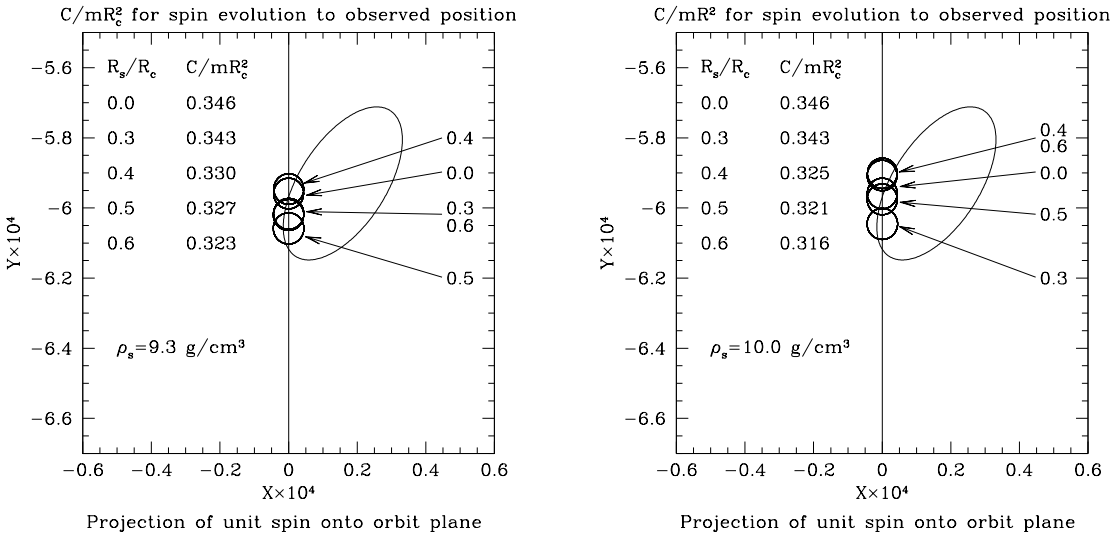

Fig. 8.— Values of C/mR_c^2 necessary to restore mantle spins to observed positions for $\rho_s = 9.3$ and 10.0 g/cm^3.

values of C/mR_c^2, which also decrease with increasing R_s. The figures equivalent to the left panels of Fig. 6 generated for the higher-density cores with $C/mR_c^2 \equiv 0.346$ resemble the left panels in Fig. 6. The details of these models are found in Table 1.

This exercise is completed for values of $R_s = 0.3$, 0.4, 0.5, 0.6, for $\rho_s = 8.0\,\mathrm{g/cm^3}$ and the values of C/mR_c^2, $(C_m + C_c)/C$, ρ_s, ρ_f, ρ_m, ϵ_s, ϵ_f, ϵ_m, ξ_s, ξ_f, ξ_m, i_s, i_f, i_m are shown in Table 1 for each choice of R_s and ρ_s. The limiting circles traced by the projections of the spin axes onto the orbit plane for each choice of R_s and consequent value of C/mR_c^2 are shown in Fig. 7, where the obliquities given in Table 1 correspond to the centers of the circles. The close grouping of the mantle spins are all within the one-standard-deviation uncertainty of the observation indicated by the ellipse. The most important results are the values of C/mR_c^2 and $(C_m + C_c)/C$ as these are crucial constraints on the interior structure. The dependence of C/mR_c^2 on the inner core size means that we can reduce the uncertainty in its value only with a future determination of the properties of the inner core.

The most important and complete information about the models is contained in Table 1. Therein are all the densities and radii of the various layers both assumed and derived for all of the models. Here is where the viability of the various models can be ascertained. Some densities may be out of bounds on the basis of geochemical constraints, and the density contrast between layers, say between the inner core and the fluid outer core, may be too small or too large. For the larger values of R_s and $\rho_s = 8.0$ g/cm^3, there is very little contrast in density between inner and outer core. Is this unreasonable? The advantage of these models is that they are consistent with the observables. Readers may then consider models that cater to their own views concerning Mercury's interior.

A model with $\rho_s = 8$ g/cm^3 would have to have rather special chemical partitioning and material properties. Due to the 5–8-fold increase in pressure across Mercury's core (e.g., Hauck II et al. 2013), the mean density difference between the inner core and outer core is driven largely by self-compression. Still, even for pure Fe the expected density difference between solid and liquid is about 4%. Thus, consistent with internal structure calculations constrained by an equation of state (Hauck II et al. 2013; Rivoldini and Van Hoolst 2013) models with inner core densities closer to 9.3g/cm^3 are more likely as are the corresponding models in Fig. 8 and Table 1. Interestingly, in those models with inner cores larger than $0.3R_c$ we infer mean mantle densities of ~ 3 g/cm^3. Whereas there is some trade-off with the crustal density, such a result is in distinct contrast with the larger densities for Mercury's mantle given in previous work (Smith et al. 2012; Hauck II et al. 2013). Regardless, such a low mean mantle density is a potential challenge to explain because it is lower even than Mg-rich olivine and Mg-rich orthopyroxene, which have densities of $3.2 - 3.3$ g/cm^3 and likely dominate Mercury's Fe-poor interior. Should the densities of such minerals be invoked to constrain the lower bound on the mantle density of the planet we would then infer that Mercury must have an inner core that is not larger than $0.3R_c$.

An interesting property of Table 1 is the relatively large and negative values of the mantle ellipticities ϵ_m and ξ_m. These ellipticities pertain to the interface between crust and mantle. The large values result from the very large contribution of the crust to J_2 and C_{22}. The mantle–crust interface is prolate instead of oblate to compensate the large crustal contribution with the long axis of the ellipsoid parallel to the spin axis. A similar distortion in the equatorial plane has the long axis of the equatorial ellipse perpendicular to the x axis. This geometry means that the crust is thinner at the poles and at the extremes of the y axis. For $\epsilon_m = 0.005$ the crust is about 12 km thinner at the poles than the average thickness of 50 km. For $\epsilon_m = 0.002$ it would be about 5 km thinner.

5. Conclusions

The influence of an inner core on Mercury's obliquity reduces our confidence in the knowledge of the moment of inertia of Mercury. If the inner core is small ($R_s/R_c < 0.35$) and our assumed range of inner core densities ($8 - 10$ g/cm^3) encompasses the actual value, then the existing estimate of $C/MR_c^2 = 0.346 \pm 0.014$ remains valid. However, if the inner core size exceeds that threshold, we will need to measure the inner core size in order to revise the estimate of the moment of inertia. Current constraints on crustal density coupled with interior structure models (Hauck II et al. 2013) seem to favor inner core sizes that do not exceed 30% of the planet radius ($R_s/R_c < 0.3$). Likewise, dynamo models that can reproduce peculiar features of Mercury's magnetic field (Cao et al. 2014) favor a small inner core ($R_s/R_f < 0.4$). A large inner core ($R_s/R_c > 0.4$) may produce detectable signatures in the 88-day librations of the planet (Van Hoolst et al. 2012), although not at the current sensitivity levels. Detecting the influence of an inner core on the long-period librations (Yseboodt et al. 2013) would likewise require higher precision observations. In order to tighten our estimates of Mercury's moment of inertia, improved measurement of the librations or measurements of the inner core size will be required. The latter is the more powerful approach and is best achieved by deploying seismometers on the surface.

6. Appendix A: Gravitational torque on inner core

Here we derive the direct gravitational torque on the inner core and the contribution of the gravity field to the pressure torque. We find that the combination of these torques is equivalent to the direct gravitational torque but for an inner core of density $\rho_s - \rho_f$. The torque due to gravity must vanish if $\rho_f = \rho_s$.

6.1. Gravitational torque

The direct gravitational torque on the inner core due to the Sun is $\mathbf{r} \times \nabla V$, where $\mathbf{r}$ is the vector distance to the Sun from Mercury's center and where

$$V = -\frac{Gm_\odot m_s}{r}\left[1 - J_{2s}\frac{R_s^2}{r^2}\left(\frac{3\cos^2\theta}{2} - \frac{1}{2}\right) + 3C_{22s}\frac{R_s^2}{r^2}\sin^2\theta\cos 2\phi\right], \tag{30}$$

is the potential of the Sun in the gravitational field of Mercury's inner core up to second spherical harmonic degree. In Eq. (30), m_s and $m_\odot$ are the masses of Mercury's inner core

and the Sun, respectively, G is the gravitational constant, R_s is the radius of Mercury's inner core, θ, ϕ are spherical polar coordinates relative to the principal axis system of the inner core, which define the direction to the Sun, and $J_{2s} = [C_s - (A_s + B_s)/2]/m_s R_s^2$ and $C_{22s} = (B_s - A_s)/(4m_s R_s^2)$ are the zonal and tesseral coefficients of degree 2 in the spherical harmonic expansion of the inner core gravitational field. $A_s < B_s < C_s$ are the principal moments of inertia of the inner core.

We determine the components of $\mathbf{r} \times \nabla V$ in spherical coordinates and make the substitutions $\hat{\mathbf{e}}_\theta = \cos\theta\cos\phi\mathbf{i}_s + \cos\theta\sin\phi\mathbf{j}_s - \sin\theta\mathbf{k}_s$ and $\hat{\mathbf{e}}_\phi = -\sin\phi\mathbf{i}_s + \cos\phi\mathbf{j}_s$, where $\hat{\mathbf{e}}_\theta$, $\hat{\mathbf{e}}_\phi$ = unit vectors in the θ and ϕ directions and $\mathbf{i}_s$, $\mathbf{j}_s$, $\mathbf{k}_s$ = unit vectors along the principal axes of the inner core, to arrive at the solar torque on the inner core

$$\begin{aligned}\mathbf{r} \times \nabla V &= \frac{Gm_\odot}{r^3}[\cos\theta\sin\theta\sin\phi m_s R_s^2(3J_{2s} - 6C_{22s})\mathbf{i}_s - \cos\theta\sin\theta\cos\phi m_s R_s^2(3J_{2s} + 6C_{22s})\mathbf{j}_s \\ &\quad +12\sin^2\theta\sin\phi\cos\phi m_s R_s^2 C_{22s}\mathbf{k}_s], \end{aligned} \tag{31}$$

For comparison with the pressure torque below, we write Eq. (31) in a different form. For a homogeneous ellipsoid, the moments of inertia about the principal axes are given by $A = M(b^2 + c^2)/5$, $B = M(a^2 + c^2)/5$, $C = M(a^2 + b^2)/5$ so that $C - A = M(a^2 - c^2)/5 = 4\pi a^2 bc(a + c)\rho[(a - c)/a]/15 \approx 8\pi\rho R^5\epsilon_a/15$ to first order in ϵ_a, where $a > b > c$ are the semiaxes of the ellipsoid. Similarly, $C - B = 8\pi\rho R^5\epsilon_b/15$ and $B - A = 8\pi\rho R^5\xi/15$. From the expressions for J_{2s} and C_{22s} we can write

$$\begin{aligned}\mathbf{r} \times \nabla V &= \frac{4\pi}{15}\frac{Gm_\odot}{r^3}\rho_s R_s^5[-(2\epsilon_s - \xi_s)P_{21}(\cos\theta)\sin\phi\mathbf{i}_s + (2\epsilon_s + \xi_s)P_{21}(\cos\theta)\cos\phi\mathbf{j}_s \\ &\quad +\xi_s P_{22}(\cos\theta)\sin 2\phi\mathbf{k}_s], \end{aligned} \tag{32}$$

where $P_{21}(\cos\theta) = -3\sin\theta\cos\theta$, and $P_{22} = 3\sin^2\theta$.

6.2. Pressure torque

Consider the fluid outer core bounded by the surfaces at the core-mantle boundary (CMB) and the inner core boundary (ICB). Then an application of the divergence theorem allows us to write for the pressure P

$$\iiint_V \mathbf{r} \times \nabla P dV = \iint_S \mathbf{r} \times \mathbf{n}' P dS = \iint_{CMB} \mathbf{r} \times \mathbf{n} P dS - \iint_{ICB} \mathbf{r} \times \mathbf{n} P dS, \tag{33}$$

where V is the volume of the fluid core, S is the total surface area consisting of the CMB and the ICB, $\mathbf{r}$ is the radius vector from the center of Mercury, $\mathbf{n}'$ is a unit normal pointing

out of the volume on both surfaces, and $\mathbf{n}$ is the unit normal pointing in the outward radial direction on both surfaces. This definition of $\mathbf{n}$ requires the negative sign on the surface integral over the ICB. From Newton's law applied to a unit volume of fluid,

$$\nabla P = -\rho_f \frac{d\mathbf{v}}{dt} - \rho_f \nabla\Phi = -\rho_f \left[\frac{\partial \mathbf{v}}{\partial t} + (\mathbf{v}\cdot\nabla)\mathbf{v} + \nabla\Phi \right], \tag{34}$$

where ρ_f is the fluid density, $\mathbf{v}$ is the fluid velocity at the point, and Φ is the gravitational potential.

The two surface integrals at the right extreme of Eq. (33) are the pressure torques exerted on the mantle and the inner core, respectively. The contribution to this pressure torque on the inner core from the gravitational potential is

$$\iint_{ICB} \mathbf{r}\times\mathbf{n}\rho_f\Phi dS, \tag{35}$$

where the potential of the Sun interior to Mercury is

$$\Phi = -\frac{Gm_\odot}{r}\sum_{l=0}^{\infty}\sum_{m=0}^{l}\left(\frac{r'}{r}\right)^l (2-\delta_{0m})\frac{(l-m)!}{(l+m)!}P_{lm}(\cos\theta)P_{lm}(\cos\theta')\cos m(\phi-\phi'), \tag{36}$$

and where r,θ,ϕ are the spherical coordinates of the Sun in the principal axis system of coordinates of the inner core, r',θ',ϕ' are the spherical coordinates of a point on the ICB with the ellipsoidal surface of the ICB represented by $r' = R_s(1-(2\epsilon_s/3)P_{20}(\cos\theta') + (\xi_s/6)P_{22}(\cos\theta')\cos 2\phi'$, and $P_{\ell m}$ are Legendre functions. Here R_s is the mean radius of the ICB and ϵ_s and ξ_s are the mean polar and equatorial ellipticities defined by $\epsilon_s = \epsilon_{sa}/2 + \epsilon_{sb}/2 = (a-c)/2a + (b-c)/2a$ and $\xi_s = (a-b)/a$, respectively, with $a>b>c$ being the principal axis radii. We can form the function

$$H = r' - R_s[1-(2\epsilon_s/3)P_{20}(\cos\theta') + (\xi_s/6)P_{22}(\cos\theta')\cos 2\phi'], \tag{37}$$

so that the surface normal is

$$\mathbf{n} = \frac{\nabla H}{|\nabla H|} = \hat{\mathbf{e}}_r - \cos\theta'\sin\theta'\left(2\epsilon_s + \xi_f\cos 2\phi\right)\hat{\mathbf{e}}_{\theta'} + \xi_s\sin\theta'\sin 2\phi'\hat{\mathbf{e}}_{\phi'}, \tag{38}$$

where $|\nabla H|$ is $\mathrm{O}(1+\epsilon_s^2 \,\mathrm{or}\, \xi_s^2)$ and

$$\mathbf{r}'\times\mathbf{n} = -R_s[\cos\theta'\sin\theta'\left(2\epsilon_s + \xi_s\cos 2\phi'\right)\hat{\mathbf{e}}_{\phi'} + \xi_s\sin\theta'\sin 2\phi'\hat{\mathbf{e}}_{\theta'}]. \tag{39}$$

Substitution of Eqs. (39) and (36) into Eq. (35) yields the pressure torque on the ICB from the solar potential. For the integration over the surface, we convert the unit vectors in spherical coordinates to unit vectors in Cartesian coordinates with $\hat{\mathbf{e}}'_\phi = -\sin\phi'\mathbf{i}_s + \cos\phi'\mathbf{j}_s$ and

$\hat{\mathbf{e}}_{\theta'} = \cos\theta'\cos\phi'\mathbf{i}_s + \cos\theta'\sin\phi'\mathbf{j}_s - \sin\theta'\mathbf{k}_s$. All the terms in the $\mathbf{i_s}$ and $\mathbf{j_s}$ components of the integrand contain the product $\cos\theta'\sin\theta'$, which selects only the $P_{21}(\cos\theta') = -3\sin\theta'\cos\theta'$ term in Φ, and the $\mathbf{k}_s$ component contains $\sin^2\theta'$, which selects only the $P_{22}(\cos\theta')$ term in Φ from the orthogonality of the Legendre functions. Integration yields

$$\begin{aligned}\mathbf{\Gamma}^s_{P\odot} &= \frac{4\pi}{15}\frac{Gm_\odot}{r^3}R_s^5\rho_f\big[(2\epsilon_s - \xi_s)P_{21}(\cos\theta)\sin\phi\mathbf{i}_s \\ &\quad -(2\epsilon_f + \xi_s)P_{21}(\cos\theta)\cos\phi\mathbf{j}_s - \xi_s P_{22}(\cos\theta)\sin 2\phi\mathbf{k}_s\big]. \qquad (40)\end{aligned}$$

The components of Eq. (40) are identical to the components in Eq. (32) except ρ_f is the factor instead of ρ_s and the sign is reversed. That means that the torque on the inner core due to the gravity field of the Sun is equivalent to the gravitational torque on the body with the shape of the inner core, but with density $\rho_s - \rho_f$. The torque vanishes if the densities are the same.

The pressure torque (Eq. (35)) on the inner core due to the internal potential of the mantle and that part of the fluid core protruding into the mantle is found in the same way. The internal potential from the material above the inner core is given in Eq. (8), and the surface density of the inner core material outside of the largest sphere that would fit within is given in Eq. (7). The internal potential can be written

$$\Phi_{int} = \frac{8\pi G}{15}K_a[z_m^2 - (x_m^2 + y_m^2)/2] - \frac{2\pi G}{5}K_b(x_m^2 - y_m^2) \qquad (41)$$

where $K_a = \epsilon_m\rho_m + \epsilon_f(\rho_f - \rho_m)$ and $K_b = \xi_m\rho_m + \xi_f(\rho_f - \rho_m)$, and where x_m, y_m, z_m are again Cartesian coordinates of a point inside the inner core along the principal axes of the mantle. The torque on the inner core from this potential is (Eq. (16))

$$\mathbf{T}_{ic} = -\iiint_V \mathbf{r}\times\rho_s\nabla\Phi dV,$$

where the integration is over the volume of the inner core.

In Section 2.2 we worked with the components of the torque along the mantle principal axes. Here it is more convenient to work with the components along the inner core principal axes for comparison with the pressure torque. To this end we transform the coordinates in Eq. (41) to the inner core frame with $x_m = \ell_1 x_s + \ell_2 y_s + \ell_3 z_s$, $y_m = m_1 x_s + m_2 y_s + m_3 z_s$, and $z_m = n_1 x_s + n_2 y_s + n_3 z_s$, which are defined in Section 2.2. $\nabla\Phi$ is now in terms of the inner core coordinate system, and $\mathbf{r} = (x_s, y_s, z_s)$. In Eq. (16) the inner core is homogeneous, so the integral over the sphere with radius R_s vanishes. Then the volume integral can be treated as a surface integral with $\rho_s dV = \rho_s\Delta r dS$ with

$$\rho_s\Delta r = \sigma_s(\theta_s,\phi_s) = -\frac{2}{3}\epsilon_s R_s\rho_s P_{20}(\cos\theta_s) + \frac{\xi_s}{6}R_s\rho_s P_{22}(\cos\theta_s)\cos 2\phi_s, \qquad (42)$$

which follows from Eq. (7). For integration over the ICB surface we change (x_s, y_s, z_s) to $(R_s \sin\theta_s \cos\phi_s,\ R_s \sin\theta_s \sin\phi_s,\ R_s \cos\theta_s)$. Then Eq. (16) becomes

$$\begin{aligned}
\mathbf{T}_{ic} &= -\int_0^{2\pi}\int_0^{\pi} \mathbf{r} \times \nabla_s \Phi \sigma_s(\theta_s, \phi_s) R_s^2 \sin\theta_s d\theta_s d\phi_s \\
&= -\frac{16}{75}\pi^2 G \rho_s R_s^5 \Big[(2\epsilon_s - \xi_s)[2K_a n_2 n_3 - K_b(\ell_2\ell_3 - m_2 m_3)]\mathbf{i}_s \\
&\quad +(2\epsilon_s + \xi_s)[-2K_a n_1 n_3 + K_b(\ell_1\ell_3 - m_1 m_3)]\mathbf{j}_s \\
&\quad +\xi_s[4K_a n_1 n_2 - 2K_b(\ell_1\ell_2 - m_1 m_2)]\mathbf{k}_s \Big]. \qquad (43)
\end{aligned}$$

The pressure torque on the inner core due to the internal potential of the mantle starts with Eq. (35), where Φ is now Eq. (41). The cross product $\mathbf{r} \times \mathbf{n}$ in Eq. (39) is converted to Cartesian components in the inner core as are the mantle system coordinates in Eq. (41). The inner core coordinates are converted to spherical polar coordinates for integration over the ICB. There results

$$\begin{aligned}
\Gamma_{_{Pmantle}} &= \int_0^{2\pi}\int_0^{\pi} \mathbf{r} \times \mathbf{n} \rho_f \Phi_{int} R_s^2 \sin\theta_s d\theta_s d\phi_s \\
&= \frac{16}{75}\pi^2 G \rho_f R_s^5 \Big[(2\epsilon_s - \xi_s)[2K_a n_2 n_3 - K_b(\ell_2\ell_3 - m_2 m_3)]\mathbf{i}_s \\
&\quad +(2\epsilon_s + \xi_s)[-2K_a n_1 n_3 + K_b(\ell_1\ell_3 - m_1 m_3)]\mathbf{j}_s \\
&\quad +\xi_s[4K_a n_1 n_2 - 2K_b(\ell_1\ell_2 - m_1 m_2)]\mathbf{k}_s \Big]. \qquad (44)
\end{aligned}$$

Eq. (44) is identical to Eq.(43) except ρ_f replaces ρ_s and the sign is reversed. Hence, the pressure torque on the inner core due the applied potentials alone opposes the direct gravitational torque for both the solar and mantle potentials and is included by the factor $\rho_s - \rho_f$ in the calculation of the direct gravitational torque on the inner core. We conjecture that this statement is true for any arbitrary potential applied to the inner core.

REFERENCES

Baland, R., van Hoolst, T., 2010. Librations of the Galilean satellites: The influence of global internal liquid layers. Icarus 209, 651–664.

Baland, R.M., van Hoolst, T., Yseboodt, M., Karatekin, Ö., 2011. Titan's obliquity as evidence of a subsurface ocean? Astron. Astrophys. 530, A141.

Cao, H., Aurnou, J.M., Wicht, J., Dietrich, W., Soderlund, K.M., Russell, C.T., 2014. A dynamo explanation for Mercury's anomalous magnetic field. Geophys. Res. Lett. 41, 4127–4134.

Colombo, G., 1966. Cassini's second and third laws. Astron. J. 71, 891–896.

Colombo, G., Shapiro, I.I., 1966. The rotation of the planet Mercury. Astrophys. J. 145, 296–307.

Correia, A.C.M., Laskar, J., 2004. Mercury's capture into the 3/2 spin-orbit resonance as a result of its chaotic dynamics. Nature 429, 848–850.

Correia, A.C.M., Laskar, J., 2009. Mercury's capture into the 3/2 spin-orbit resonance including the effect of core-mantle friction. Icarus 201, 1–11.

Correia, A.C.M., Laskar, J., 2012. Impact cratering on Mercury: Consequences for the spin evolution. Astrophys. J. 751, L43.

Goldreich, P., Peale, S., 1966. Spin-orbit coupling in the solar system. Astron. J. 71, 425–438.

Goldstein, H., 1980. Classical Mechanics. 2nd ed., Addison-Wesley.

Hauck II, S.A., Margot, J.L., Solomon, S.C., Phillips, R.J., Johnson, C.L., Lemoine, F.G., Mazarico, E., McCoy, T.J., Padovan, S., Peale, S.J., Perry, M.E., Smith, D.E., Zuber, M.T., 2013. The curious case of Mercury's internal structure. J. Geophys. Res. 118, 1204–1220.

Margot, J.L., Peale, S.J., Jurgens, R.F., Slade, M.A., Holin, I.V., 2007. Large longitude libration of Mercury reveals a molten core. Science 316, 710–714.

Margot, J.L., Peale, S.J., Solomon, S.C., Hauck II, S.A., Ghigo, F.D., Jurgens, R.F., Yseboodt, M., Giorgini, J.D., Padovan, S., Campbell, D.B., 2012. Mercury's moment of inertia from spin and gravity data. J. Geophys. Res. 117. doi:10.1029/2012JE004161.

Mazarico, E., Genova, A., Goossens, S., Lemoine, F.G., Neumann, G.A., Zuber, M.T., Smith, D.E., Solomon, S.C., 2014. The gravity field, orientation, and ephemeris of Mercury from MESSENGER observations after three years in orbit. J. Geophys. Res. Planets 119, 2417–2436.

Melchior, P., 1986. The Physics of the Earth's Core. Pergamon Press.

Noyelles, B., Frouard, J., Makarov, V.V., Efroimsky, M., 2014. Spin-orbit evolution of Mercury revisited. Icarus 241, 26–44.

Padovan, S., Wieczorek, M.A., Margot, J.L., Tosi, N., Solomon, S.C., 2015. Thickness of the crust of Mercury from geoid-to-topography ratios. Geophys. Res. Lett. 42, 1029–1038.

Peale, S.J., 1969. Generalized Cassini's laws. Astron. J. 74, 483–489.

Peale, S.J., 1974. Possible histories of the obliquity of Mercury. Astron. J. 79, 722–744.

Peale, S.J., 2005. The free precession and libration of Mercury. Icarus 178, 4–18.

Peale, S.J., 2006. The proximity of Mercury's spin to Cassini state 1 from adiabatic invariance. Icarus 181, 338–347.

Peale, S.J., Margot, J.L., Hauck II, S.A., Solomon, S.C., 2014. Effect of core-mantle and tidal torques on Mercury's spin axis orientation. Icarus 231, 206–220.

Perry, M.E., Neumann, G.A., Phillips, R.J., Barnouin, O.S., Ernst, C.M., Kahan, D.S., Solomon, S.C., Zuber, M.T., Smith, D.E., II, S.A.H., Peale, S.J., Margot, J.L., Mazarico, E., Johnson, C.L., Gaskell, R.W., Roberts, J.H., Jr., R.L.M., Oberst, J., 2015. The low-degree shape of Mercury. Geophys. Res. Lett. 42. doi:10.1002/2015GL065101.

Pettengill, G.H., Dyce, R.B., 1965. A radar determination of the rotation of the planet Mercury. Nature 206, 1240.

Poincaré, H., 1910. Sur la précession des corps déformables. Bull. Astron. 27, 321–367.

Rivoldini, A., Van Hoolst, T., 2013. The interior structure of Mercury constrained by the low-degree gravity field and the rotation of Mercury. Earth Planet. Sci. Lett. 377, 62–72.

Smith, D.E., Zuber, M.T., Phillips, R.J., Solomon, S.C., Hauck II, S.A., Lemoine, F.G., Mazarico, E., Neumann, G.A., Peale, S.J., Margot, J.L., Johnson, C.L., Torrence, M.H., Perry, M.E., Rowlands, D.D., Goossens, S., Head, J.W., Taylor, A.H., 2012.

Gravity field and internal structure of Mercury from MESSENGER. Science 336, 214–217.

Stark, A., Oberst, J., Preusker, F., Peale, S.J., Margot, J.L., Phillips, R.J., Neumann, G.A., Smith, D.E., Zuber, M.T., Solomon, S.C., 2015. First MESSENGER orbital observations of Mercury's librations. Geophys. Res. Lett. 42. doi:10.1002/2015GL065152.

Szeto, A.M.K., Xu, S., 1997. Gravitational coupling in a triaxial ellipsoidal Earth. J. Geophys. Res. 102, 27651–27658.

Van Hoolst, T., Rivoldini, A., Baland, R.M., Yseboodt, M., 2012. The effect of tides and an inner core on the forced longitudinal libration of Mercury. Earth Planet. Sci. Lett. 333, 83–90.

Wieczorek, M.A., Correia, A.C.M., Le Feuvre, M., Laskar, J., Rambaux, N., 2012. Mercury's spin-orbit resonance explained by initial retrograde and subsequent synchronous rotation. Nature Geosci. 5, 18–21.

Wieczorek, M.A., Neumann, G.A., Nimmo, F., Kiefer, W.S., Taylor, G.J., Melosh, H.J., Phillips, R.J., Solomon, S.C., Andrews-Hanna, J.C., Asmar, S.W., Konopliv, A.S., Lemoine, F.G., Smith, D.E., Watkins, M.M., Williams, J.G., Zuber, M.T., 2013. The crust of the Moon as seen by GRAIL. Science 339, 671–675.

Yseboodt, M., Margot, J.L., 2006. Evolution of Mercury's obliquity. Icarus 181, 327–337.

Yseboodt, M., Rivoldini, A., Van Hoolst, T., Dumberry, M., 2013. Influence of an inner core on the long-period forced librations of Mercury. Icarus 226, 41–51.

Table 1: Values of densities, radii, obliquities, and ellipticities for all the models.

Parameters versus inner core size and density

R_s/R	C/MR^2	C_m/C	ρ_s g/cm^3	ρ_f g/cm^3	ρ_m g/cm^3	ρ_c g/cm^3	R_f km	R_m km	$i_m{}'$	$i_f{}'$	$i_s{}'$
0.0	0.346	0.431	-	7.237	3.285	2.8	1999	2390	2.05	5.65	-
0.3	0.346	0.431	8.0	7.152	3.311	2.8	2004	2390	2.06	5.33	5.42
0.4	0.340	0.439	8.0	7.372	3.174	2.8	1979	2390	2.06	4.68	4.91
0.5	0.334	0.446	8.0	7.682	3.035	2.8	1949	2390	2.04	4.24	4.50
0.6	0.332	0.449	8.05	7.996	2.939	2.8	1926	2390	2.08	1.77	3.54
0.3	0.343	0.435	9.3	7.156	3.272	2.8	1997	2390	2.07	4.89	5.15
0.4	0.330	0.452	9.3	7.618	3.007	2.8	1943	2390	2.04	3.61	4.16
0.5	0.327	0.456	9.3	7.335	3.011	2.8	1944	2390	2.08	2.18	3.06
0.6	0.323	0.462	9.3	6.671	3.023	2.8	1947	2390	2.07	1.51	2.41
0.3	0.343	0.435	10.0	7.077	3.295	2.8	2000	2390	2.08	4.69	5.06
0.4	0.325	0.459	10.0	7.742	2.933	2.8	1925	2390	2.03	3.18	3.88
0.5	0.321	0.465	10.0	7.355	2.960	2.8	1925	2390	2.05	1.82	2.84
0.6	0.316	0.472	10.0	6.386	2.960	2.8	1931	2390	2.03	1.27	2.29

Ellipticities

ρ_sg/cm^3	R_s/R	ϵ_s	ϵ_f	ϵ_m	ϵ_c	ξ_s	ξ_f	ξ_m	ξ_c
-	0.0	-	6.047×10^{-5}	-2.183×10^{-3}	5.534×10^{-4}	-	3.464×10^{-5}	-2.260×10^{-3}	4.919×10^{-4}
8.0	0.3	5.800×10^{-5}	6.043×10^{-5}	-2.070×10^{-3}	5.534×10^{-4}	3.322×10^{-5}	3.461×10^{-5}	-2.144×10^{-3}	4.919×10^{-4}
8.0	0.4	5.835×10^{-5}	5.981×10^{-5}	-2.832×10^{-3}	5.534×10^{-4}	3.342×10^{-5}	3.426×10^{-5}	-2.931×10^{-3}	4.919×10^{-4}
8.0	0.5	5.865×10^{-5}	5.916×10^{-5}	-4.513×10^{-3}	5.534×10^{-4}	3.359×10^{-5}	3.389×10^{-5}	-4.668×10^{-3}	4.919×10^{-4}
8.0	0.6	5.858×10^{-5}	5.890×10^{-5}	-5.197×10^{-3}	5.534×10^{-4}	3.355×10^{-5}	3.374×10^{-5}	-5.377×10^{-3}	4.919×10^{-4}
9.3	0.3	5.438×10^{-5}	6.008×10^{-5}	-2.240×10^{-3}	5.534×10^{-4}	3.115×10^{-5}	3.441×10^{-5}	-2.231×10^{-3}	4.919×10^{-4}
9.3	0.4	5.510×10^{-5}	5.856×10^{-5}	-5.107×10^{-3}	5.534×10^{-4}	3.156×10^{-5}	3.355×10^{-5}	-5.289×10^{-3}	4.919×10^{-4}
9.3	0.5	5.514×10^{-5}	5.806×10^{-5}	-4.991×10^{-3}	5.534×10^{-4}	3.158×10^{-5}	3.326×10^{-5}	-5.178×10^{-3}	4.919×10^{-4}
9.3	0.6	5.517×10^{-5}	5.738×10^{-5}	-4.694×10^{-3}	5.534×10^{-4}	3.160×10^{-5}	3.287×10^{-5}	-4.881×10^{-3}	4.919×10^{-4}
10.0	0.3	5.250×10^{-5}	6.005×10^{-5}	-2.131×10^{-3}	5.534×10^{-4}	3.007×10^{-5}	3.439×10^{-5}	-2.209×10^{-3}	4.919×10^{-4}
10.0	0.4	5.350×10^{-5}	5.786×10^{-5}	-7.929×10^{-3}	5.534×10^{-4}	3.065×10^{-5}	3.314×10^{-5}	-8.216×10^{-3}	4.919×10^{-4}
10.0	0.5	5.351×10^{-5}	5.715×10^{-5}	-7.723×10^{-3}	5.534×10^{-4}	3.065×10^{-5}	3.274×10^{-5}	-8.020×10^{-3}	4.919×10^{-4}
10.0	0.6	5.347×10^{-5}	5.625×10^{-5}	-6.539×10^{-3}	5.534×10^{-4}	3.063×10^{-5}	3.222×10^{-5}	-6.813×10^{-3}	4.919×10^{-4}